MULTISCALE MODEL. SIMUL.
Vol. 21, No. 1, pp. 218-268

POTENTIAL SINGULARITY FORMATION OF INCOMPRESSIBLE AXISYMMETRIC EULER EQUATIONS WITH DEGENERATE VISCOSITY COEFFICIENTS*

THOMAS Y. HOU† AND DE HUANG‡

Abstract. In this paper, we present strong numerical evidence that the incompressible axisymmetric Euler equations with degenerate viscosity coefficients and smooth initial data of finite energy develop a potential finite-time locally self-similar singularity at the origin. An important feature of this potential singularity is that the solution develops a two-scale traveling wave that travels toward the origin. The two-scale feature is characterized by the scaling property that the center of the traveling wave is located at a ring of radius $O((T-t)^{1/2})$ surrounding the symmetry axis while the thickness of the ring collapses at a rate $O(T-t)$. The driving mechanism for this potential singularity is due to an antisymmetric vortex dipole that generates a strong shearing layer in both the radial and axial velocity fields. Without the viscous regularization, the three-dimensional Euler equations develop a sharp front and some shearing instability in the far field. On the other hand, the Navier–Stokes equations with a constant viscosity coefficient regularize the two-scale solution structure and do not develop a finite-time singularity for the same initial data.

Key words. potential singularity, Navier–Stokes equations, Euler equations, multiscale blowup, degenerate viscosity

MSC codes. 35Q30, 35Q31, 35A21

DOI. 10.1137/22M1470906

1. Introduction.

The three-dimensional (3D) incompressible Euler equations in fluid dynamics describe the motion of inviscid incompressible flows. Despite their wide range of applications, the question regarding the global regularity of the 3D Euler equations with smooth initial data of finite energy has remained open [MB02]. The main difficulty associated with the global regularity of the 3D Euler equations is the presence of vortex stretching, which is absent in the corresponding 2D problem. In 2014, Luo and Hou [LH14a, LH14b] presented strong numerical evidence that the 3D axisymmetric Euler equations with smooth initial data and boundary develop potential finite-time singular solutions at the boundary. The presence of the boundary and the symmetry properties of the initial data seem to play a crucial role in generating a sustainable finite-time singularity of the 3D Euler equations.

In this paper, we present strong numerical evidence that the incompressible axisymmetric Euler equations with smooth degenerate viscosity coefficients and smooth initial data of finite energy seem to develop a two-scale locally self-similar singularity. Unlike the Hou–Luo blowup scenario, the potential singularity for the Euler equations with degenerate viscosity coefficients occurs at the origin. Without the viscous regularization, the 3D Euler equations develop an additional small scale characterizing

* Received by the editors January 11, 2022; accepted for publication (in revised form) October 7, 2022; published electronically February 25, 2023.
https://doi.org/10.1137/22M1470906
Funding: This research was in part supported by NSF grants DMS-1907977 and DMS-1912654. The second author was supported by the National Key R&D Program of China under grant 2021YFA1001500 and received support from the Choi Family Postdoc Gift Fund.

† Applied and Computational Mathematics, Caltech, Pasadena, CA 91125 USA (hou@cms.caltech.edu).
‡ School of Mathematical Sciences, Peking University, Beijing, China (dhuang@math.pku.edu.cn).

the thickness of the sharp front. The degenerate viscosity coefficients are designed to select a stable locally self-similar two-scale solution structure and stabilize the shearing induced instability in the far field.

We also study the Navier–Stokes equations with a constant viscosity coefficient using the same initial data. Our study shows that the Navier–Stokes equations will regularize the two-scale solution structure and destroy the strong nonlinear alignment of the vortex stretching term. Moreover, we will present some preliminary numerical results indicating that the 3D Euler equations seem to develop a three-scale solution structure. The rapid collapse of the thickness of the sharp front makes it extremely difficult to resolve the potential Euler singularity numerically.

1.1. Major features of the potential blowup and the blowup mechanism. One of the important features of the potential blowup solution is that it develops a two-scale traveling solution approaching the origin. We denote by u^θ and ω^θ the angular velocity and the angular vorticity, respectively, and define $u_1 = u^\theta/r$ and $\omega_1 = \omega^\theta/r$ with $r = \sqrt{x^2+y^2}$. Let $(R(t), Z(t))$ be the location where u_1 achieves its global maximum in the rz-plane. The traveling wave is centered at a ring with radius $R(t)$ surrounding the symmetry axis $r = 0$ and the thickness of the ring is roughly of order $Z(t)$. The two-scale traveling wave solution is characterized by the scaling property that $R(t) = O((T-t)^{1/2})$ and $Z(t) = O(T-t)$. Another important feature is that the odd symmetry (in z) of the initial data of ω_1 induces a vortex dipole and an antisymmetric local convective circulation. This convective circulation is the cornerstone of our blowup scenario, as it has the desirable property of pushing the solution near $z = 0$ toward the symmetry axis $r = 0$.

An important guiding principle for constructing our initial data is to enforce a strong nonlinear alignment of vortex stretching. First of all, the vortex dipole induces a negative radial velocity u^r near $z = 0$, i.e., $u^r = -r\psi_{1,z} < 0$, which implies $\psi_{1,z} > 0$. Moreover, $\psi_{1,z}(R(t), z, t)$ is a monotonically decreasing function of z and is relatively flat near $z = 0$. Through the vortex stretching term $2\psi_{1,z}u_1$ (see (2.2a)), the large value of $\psi_{1,z}$ near $z = 0$ induces a traveling wave for u_1 that approaches $z = 0$ rapidly. The strong nonlinear alignment in vortex stretching overcomes the stabilizing effect of advection in the upward z direction (see, e.g., [HL08a, HL09]). The oddness of u_1 in z then generates a large positive gradient u_{1z}, which contributes positively to the rapid growth of ω_1 through the vortex stretching term $2u_1u_{1z}$ (see (2.2b)). The rapid growth of ω_1 in turn feeds back to the rapid growth of $\psi_{1,z}$. The whole coupling mechanism described above forms a positive feedback loop.

Moreover, we observe that the 2D velocity field $(u^r(t), u^z(t))$ in the rz-plane forms a closed circle right above $(R(t), Z(t))$. The corresponding streamline is then trapped in the circle region in the rz-plane. This local circle structure of the 2D velocity field is critical in stabilizing the blowup process, as it keeps the bulk parts of the u_1, ω_1 profiles traveling toward the origin instead of being pushed upward. The strong shear layer in u^r and u^z generates a sharp front for u_1 in both the r and z directions.

Another important feature of our initial data is that it generates a local hyperbolic flow in the rz-plane. Due to the odd symmetry of u_1, u_1 is almost zero in the region near $z = 0$. The strong upward transport near $r = 0$ makes u_1 really small in a no-spinning region between the sharp front of u_1 and the symmetry axis $r = 0$. Within this no-spinning region, the angular velocity $u^\theta = ru_1$ is almost zero, which implies that there is almost no spinning around the symmetry axis. The flow effectively travels upward along the vertical direction inside this no-spinning region. Outside this no-spinning region, u_1 becomes very large and the flow spins rapidly around the

symmetry axis. Moreover, the streamlines induced by the velocity field travel upward along the vertical direction and then move outward along the radial direction. The local blowup solution resembles the structure of a tornado. For this reason, we also call the potential singularity of the Euler equations with variable viscosity coefficients "a tornado singularity."

1.2. Asymptotic scaling analysis. To confirm that the potential singular solution develops a locally self-similar blowup, we perform numerical fitting of the growth rates for several physical quantities. Our study shows that the maximum of the vorticity vector grows like $O((T-t)^{-3/2})$, and $R(t)=O((T-t)^{1/2})$, $Z(t)=O(T-t)$. The fact that $\|\nabla \boldsymbol{u}\|_{L^\infty} \geq \|\nabla \boldsymbol{\omega}\|_{L^\infty} \geq C_0(T-t)^{-3/2}$ gives that $\int_0^T \|\nabla \boldsymbol{u}(t)\|_{L^\infty} dt = \infty$, which implies that the solution could potentially develop a finite-time singularity [MB02].

We have also performed an asymptotic scaling analysis to study the scaling properties of a potential locally self-similar blowup solution. By balancing the scales in various terms, we show that u_1 and $\psi_{1,z}$ must blow up with the rate $O(1/(T-t))$ if there is a locally self-similar blowup. Due to the conservation of total circulation $\Gamma = r^2 u_1$ and the degeneracy of the viscosity coefficients, we show that Γ remains $O(1)$ at $(R(t), Z(t))$. This property and the scaling property that $u_1 = O(1/(T-t))$ imply that $R(t) = O((T-t)^{1/2})$. Moreover, the balance between the vortex stretching term and the degenerate viscosity term suggests that $Z(t) = O(T-t)$. Similarly, we can show that ω_1 blows up like $O(1/(T-t)^2)$. In terms of the original physical variables, the vorticity vector blows up like $O(1/(T-t)^{3/2})$ and the velocity field blows up like $O(1/(T-t)^{1/2})$. The results obtained by our scaling analysis are consistent with our numerical fitting of the blowup rates for various quantities.

1.3. Comparison with results obtained in two subsequent papers. Inspired by the work presented in this manuscript, the first author of this paper investigated potential singular behavior of the 3D Euler and Navier–Stokes equations using a different but relatively simple initial condition in two subsequent papers [Hou21a, Hou21b]. Although the solution presented in this paper and the solutions obtained in [Hou21a, Hou21b] share many similar properties, there are some important differences between the two blowup scenarios. One important difference is that the potential Euler singularity considered in [Hou21a] is essentially a one-scale traveling wave singularity instead of a two-scale traveling wave singularity considered in this paper. More importantly, the scaling properties of the potential Euler singularity presented in [Hou21a] are compatible with those of the Navier–Stokes equations. In [Hou21b], it is shown that the maximum vorticity of the Navier–Stokes equations using a relatively large constant viscosity coefficient $\nu = 5 \times 10^{-3}$ increases by a factor of 10^7 relatively to its initial maximum vorticity. In comparison, the maximum vorticity of the Navier–Stokes equations with $\nu = 10^{-5}$ using the initial condition considered in this paper has increased less than 2. Another important feature of the initial condition considered in [Hou21a, Hou21b] is that it decays rapidly in the far field. As a result, its solution does not suffer from the shearing instability that we observe in this paper and there is no need to use a degenerate viscosity or a low pass filter to stabilize the shearing instability in the far field as we did in this paper.

1.4. Review of related works in the literature. One of the best known results for the 3D Euler equations is the Beale–Kato–Majda non-blowup criteria [MB02], which states that the smooth solution of the 3D Euler equations ceases to be regular at some finite time T if and only if $\int_0^T \|\nabla \boldsymbol{\omega}\|_{L^\infty} dt = \infty$. In [CFM96], Constantin, Fefferman, and Majda showed that the local geometric regularity of the vorticity

vector near the region of maximum vorticity could lead to the dynamic depletion of vortex stretching, thus preventing a potential finite-time singularity (see also [DHY05]). An exciting recent development is the work by Elgindi [Elg21] (see also [EGM21]), who proved that the 3D axisymmetric Euler equations develop a finite-time singularity for a class of $C^{1,\alpha}$ initial velocity with no swirl. There have been a number of very interesting results inspired by the Hou–Lou blowup scenario [LH14a, LH14b]; see, e.g., [KS14, CHK+17, KRYZ16, CH21, CHH21] and the excellent survey article [Kis18, DE22].

There have been a number of previous attempts to search for potential Euler singularities numerically. In [GS91], Grauer and Sideris presented numerical evidence that the 3D axisymmetric Euler equations with a smooth initial condition could develop a potential finite-time singularity away from the symmetry axis. In [ES94], E and Shu studied the potential development of finite-time singularities in the 2D Boussinesq equations with initial data completely analogous to those of [GS91, PS92] and found no evidence for singular solutions. Another well-known work on potential Euler singularity is the two antiparallel vortex tube computation by Kerr in [Ker93]. In [HL06], Hou and Li repeated the computation of [Ker93] with higher resolutions and only observed double exponential growth of the maximum vorticity in time. In [BP94], Boratav and Pelz presented numerical evidence that the 3D Euler equations with Kida's high-symmetry initial data would develop a finite-time singularity. In [HL08b], Hou and Li also repeated the computation of [BP94] and found that the singularity reported in [BP94] is likely an artifact due to underresolution. In [BHP16], Brenner, Hormoz, and Pumir considered an iterative mechanism for potential singularity formation of the 3D Euler equations. We refer to an excellent review paper [Gib08] for more discussion on potential Euler singularities.

The rest of the paper is organized as follows. In section 2, we describe the setup of the problem in some detail, including the analytic construction of our initial data and the variable viscosity coefficients. In section 3, we report the major findings of our numerical results, including the first sign of singularity and the main features of the potentially singular solution. In sections 4 and 5, we present a comparison study with the standard Navier–Stokes equations with constant viscosity coefficient and the inviscid Euler equations, respectively. In section 6, we investigate the asymptotic blowup scaling both numerically and by asymptotic scaling analysis. Some concluding remarks are made in section 7.

2. Description of the problem. We study the 3D incompressible Euler equations with (degenerate) variable viscosity coefficients:

$$\begin{aligned} \boldsymbol{u}_t + \boldsymbol{u}\cdot\nabla\boldsymbol{u} &= -\nabla p + \nabla\cdot(\nu\nabla\boldsymbol{u}), \\ \nabla\cdot\boldsymbol{u} &= 0, \end{aligned} \tag{2.1}$$

where $\boldsymbol{u} = (u^x, u^y, u^z)^T : \mathbb{R}^3 \mapsto \mathbb{R}^3$ is the 3D velocity vector, $p : \mathbb{R}^3 \mapsto \mathbb{R}$ is the scalar pressure, $\nabla = (\partial_x, \partial_y, \partial_z)^T$ is the gradient operator in $\mathbb{R}^3$, and $\nu : \mathbb{R}^3 \mapsto \mathbb{R}^{3\times 3}$ is the variable viscosity tensor. In the inviscid case (i.e., $\nu = \mathbf{0}$), (2.1) reduce to the 3D Euler equations.

2.1. Axisymmetric Euler equations. We will study the potential singularity formulation in the axisymmetric scenario. In this case, it is more convenient to rewrite equations (2.1) in the cylindrical coordinates. Consider the change of variables

$$x = r\cos\theta, \quad y = r\sin\theta, \quad z = z,$$

and the decomposition

$$\boldsymbol{v}(r,z) = v^r(r,z)\boldsymbol{e}_r + v^\theta(r,z)\boldsymbol{e}_\theta + v^z(r,z)\boldsymbol{e}_z,$$

$$\boldsymbol{e}_r = \frac{1}{r}(x,y,0)^T, \quad \boldsymbol{e}_\theta = \frac{1}{r}(-y,x,0)^T, \quad \boldsymbol{e}_z = (0,0,1)^T,$$

for radially symmetric vector-valued functions $\boldsymbol{v}(r,z)$.

The 3D Euler equations can be rewritten in the axisymmetric form. We denote by u^θ, ω^θ, ψ^θ the angular velocity, the angular vorticity, and the angular stream function, respectively. To remove the formal singularity induced by the cylindrical coordinate, Hou and Li [HL08a] introduced the variables

$$u_1 = u^\theta/r, \quad \omega_1 = \omega^\theta/r, \quad \psi_1 = \psi^\theta/r.$$

The Euler equations (2.1) with variable viscosity coefficients can be transformed into an equivalent form of these new variables in the axisymmetric case:

$$u_{1,t} + u^r u_{1,r} + u^z u_{1,z} = 2u_1\psi_{1,z} + f_{u_1}, \tag{2.2a}$$

$$\omega_{1,t} + u^r \omega_{1,r} + u^z \omega_{1,z} = 2u_1 u_{1,z} + f_{\omega_1}, \tag{2.2b}$$

$$-\left(\partial_r^2 + \frac{3}{r}\partial_r + \partial_z^2\right)\psi_1 = \omega_1, \tag{2.2c}$$

$$u^r = -r\psi_{1,z}, \quad u^z = 2\psi_1 + r\psi_{1,r}, \tag{2.2d}$$

where the f_{u_1} and f_{ω_1} are the viscosity terms.

To determine the viscosity terms, we choose the variable viscosity tensor such that

$$\nu = \mathrm{diag}(\nu^r, \nu^r, \nu^z)$$

in the cylindrical coordinates, where $\nu^r = \nu^r(r,z), \nu^z = \nu^z(r,z)$ are functions of (r,z). We remark that this is equivalent to choosing $\nu = \mathrm{diag}(\nu^x, \nu^y, \nu^z)$ with $\nu^x = \nu^y = \nu^r$ in the Euclidean coordinates $(x,y,z) = (r\cos\theta, r\sin\theta, z)$. In order for ν to be a smooth function in the primitive coordinates (x,y,z), we require that $\nu^r(r,z), \nu^z(r,z)$ are even functions of r with respect to $r = 0$. In particular, we will construct v^r, v^z in Appendix A.2 so that they are both degenerate at the origin $(r,z) = (0,0)$ of order $O(r^2) + O(z^2)$. With this choice of the variable viscosity coefficients, f_{u_1} and f_{ω_1} have the expressions

$$f_{u_1} = \nu^r\left(u_{1,rr} + \frac{3}{r}u_{1,r}\right) + \nu^z u_{1,zz} + \frac{1}{r}\nu^r_r u_1 + \nu^r_r u_{1,r} + \nu^z_z u_{1,z}, \tag{2.3a}$$

$$\begin{aligned} f_{\omega_1} = {} & \nu^r\left(\omega_{1,rr} + \frac{3}{r}\omega_{1,r}\right) + \nu^z\omega_{1,zz} + \frac{1}{r}\nu^r_r\omega_1 + \nu^r_r\omega_{1,r} + \nu^z_z\omega_{1,z} \\ & + \frac{1}{r}\left(\nu^r_z\left(u^r_{rr} + \frac{1}{r}u^r_r - \frac{1}{r^2}u^r\right) + \nu^z_z u^r_{zz} - \nu^r_r\left(u^z_{rr} + \frac{1}{r}u^z_r\right) - \nu^z_r u^z_{zz}\right) \\ & + \frac{1}{r}\Big(\nu^r_{rz}u^r_r + \nu^z_{zz}u^r_z - \nu^r_{rr}u^z_r - \nu^z_{rz}u^z_z\Big). \end{aligned} \tag{2.3b}$$

Note that v^r_r is an odd function of r; thus the term v^r_r/r is well defined as long as v^r is smooth. This also applies to the other terms with a factor $1/r$ in the expressions above.

2.2. Settings of the solution. We will solve the transformed equations (2.2) in the cylinder region

$$\mathcal{D} = \{(r,z) : 0 \le r \le 1\}.$$

In particular, we will enforce the following properties of the solution:

1. u_1, ω_1, ψ_1 are periodic in z with period 1:

$$u_1(r,z,t) = u_1(r,z+1,t), \quad \omega_1(r,z,t) = \omega_1(r,z+1,t),$$
$$\text{and} \quad \psi_1(r,z,t) = \psi_1(r,z+1,t) \quad \text{for all } (r,z) \in \mathcal{D}. \tag{2.4a}$$

2. u_1, ω_1, ψ_1 are odd functions of z at $z = 0$:

$$u_1(r,z,t) = -u_1(r,-z,t), \quad \omega_1(r,z,t) = -\omega_1(r,-z,t),$$
$$\text{and} \quad \psi_1(r,z,t) = -\psi_1(r,-z,t) \quad \text{for all } (r,z) \in \mathcal{D}. \tag{2.4b}$$

3. The smoothness of the solution in the Cartesian coordinates implies that $u^\theta, \omega^\theta, \psi^\theta$ must be an odd function of r [LW06]. Consequently, u_1, ω_1, ψ_1 must be even functions of r at $r = 0$, which imposes the pole conditions:

$$u_{1,r}(0,z) = \omega_{1,r}(0,z) = \psi_{1,r}(0,z) = 0. \tag{2.4c}$$

4. The velocity satisfies a no-flow boundary condition on the solid boundary $r = 1$:

$$\psi_1(1,z,t) = 0 \quad \text{for all } z. \tag{2.4d}$$

5. Due to the existence of nondegenerate viscosity at $r = 1$, the tangent flows on the solid boundary should satisfy a no-slip boundary condition:

$$u^\theta(1,z,t) = u^z(1,z,t) = 0 \quad \text{for all } z. \tag{2.4e}$$

In view of (2.2d) and (2.4d), this further leads to $\psi_{1,r}(1,z,t) = 0$. Therefore, the no-slip boundary in terms of the new variables u_1, ω_1, ψ_1 reads

$$u_1(1,z,t) = 0, \quad \omega_1(1,z,t) = -\psi_{1,rr}(1,z,t) \quad \text{for all } z. \tag{2.4f}$$

In fact, equations (2.2) automatically preserve properties 1–4 of the solution for all time $t \ge 0$ if the initial data satisfy these properties and if the variable viscosity coefficients v^r, v^z satisfy

i. v^r, v^z are periodic in z with period 1,
ii. v^r, v^z are even functions of z at $z = 0$,
iii. v^r, v^z are even functions of r at $r = 0$.

The no-slip boundary condition 5 will be enforced numerically. By the periodicity and the odd symmetry of the solution, we only need to solve equations (2.2) in the half-period domain

$$\mathcal{D}_1 = \{(r,z) : 0 \le r \le 1, 0 \le z \le 1/2\}.$$

Note that the properties (2.4a) and (2.4b) together imply that u_1, ω_1, ψ_1 are also odd functions of z at $z = 1/2$. The boundaries of $\mathcal{D}_1$ then behave like "impermeable walls" since

$$u^r = -r\psi_{1,z} = 0 \quad \text{on } r = 1 \quad \text{and} \quad u^z = 2\psi_1 + r\psi_{1,r} = 0 \quad \text{on } z = 0, 1/2.$$

We will solve the axisymmetric Euler equations (2.2) with degenerate viscosity coefficients and a specially designed initial condition. The construction of the initial data and the variable viscosity coefficients will be provided in detail in Appendix A. An overall description of the numerical methods will be provided in Appendix B.

For the sake of comparison, we will also study the solution of the 3D Euler equations and of the original Navier–Stokes equations with constant viscosity coefficient on the entire domain. We will compare the numerical results from different choices of viscosity coefficients to study the effect of viscosity in the potential singularity near the symmetry axis $r = 0$. As a preview, the geometric structure of the solution without viscosity quickly becomes too singular to resolve, while there is no blowup observed for the solution of the Navier–Stokes equations with a constant viscosity coefficient. This verifies the criticality of degeneracy in the viscosity coefficients.

2.3. Computational challenges. The two-scale nature of the potential singular solution presents considerable challenges in obtaining a well-resolved numerical solution for the Euler equations with variable viscosity coefficients. To resolve this potential two-scale singular solution, we design an adaptive mesh by constructing two adaptive mesh maps for r and z explicitly. More specifically, we construct our mapping densities in the near field (phase 1: resolving the $Z(t)$ scale), the intermediate field (phase 2: resolving the $R(t)$ scale), and the far field (phase 3: resolving the $O(1)$ scale) with a transition phase in between. We then allocate a fixed number of grid points in each phase and update the mesh maps dynamically according to some criteria. This adaptive mesh strategy achieves a highly adaptive mesh with the smallest mesh size of order $O(10^{-10})$. Our adaptive mesh strategy is more complicated than the one presented in [LH14a, LH14b] since we have a two-scale traveling wave.

We use a second-order finite difference method to discretize the spatial derivatives and a second-order explicit Runge–Kutta method to discretize in time. We choose an adaptive time-step size according to the standard time-stepping stability constraint with the smallest time-step size of order $O(10^{-11})$. We adopt the second-order B-spline based Galerkin method developed in [LH14a, LH14b] to solve the Poisson equation for the stream function. We also design a second-order filtering scheme to control some mild oscillations in the tail region. The overall method is second-order accurate. We have performed a resolution study in Appendix C to confirm that our method indeed gives second-order accuracy in the maximum norm.

3. Numerical results: Features of singularity. We have numerically solved the initial-boundary value problem (2.2)–(2.4) and (A.1) on the half-period cylinder $\mathcal{D}_1 = \{(r, z) : 0 \le r \le 1, 0 \le z \le 1/2\}$ with meshes of size $(n, m) = (256p, 128p)$ for $p = 2, 3, \ldots, 8$. In particular, we have performed computations in three cases:

Case 1: ν^r, ν^z given by (A.3).
Case 2: $\nu^r = \nu^z = \mu$ for some constant μ.
Case 3: $\nu^r = \nu^z = 0$.

We will focus our discussions on the potential blowup phenomena in Case 1. Our results suggest that the solution will develop a singularity on the symmetry axis $r = 0$ in finite time, and we will provide ample evidence to support this finding. We first present, in this section, the major features of the potential finite-time singularity revealed by our computation. In Appendix C, we carry out a resolution study on the numerical solutions. Then we further quantitatively investigate the properties of the potential singularity and analyze the potential blowup scaling properties in section 6.

Cases 2 and 3 are mainly for comparison purposes. Case 2 compares the solution of the original Navier–Stokes equations and the solution of the Euler equations with degenerate viscosity coefficients using the same initial data. The results in Case 2 show that the degeneracy of the viscosity coefficients near $(r, z) = (0, 0)$ is critical for a sustainable singularity that approaches the symmetry axis $r = 0$. The corresponding numerical results and discussions are presented in section 4.

In Case 3, we study the evolution of the solution to the 3D Euler equations from the same initial data. We will see that the solutions in Case 1 and Case 3 evolve almost in the same way during the early stage of the computation. However, the Euler solution quickly develops some oscillations due to underresolution and shearing instability that prevent us from pushing the computation to the stable phase of the solution. Note that we did not apply any numerical regularization in Case 3 to suppress the instabilities. Based on our preliminary results, we conjecture that the Euler solution will develop a similar or even more singular behavior in a later stage. However, our current adaptive mesh strategy does not allow us to resolve the potential Euler singularity to reach a convincing conclusion.

3.1. Profile evolution. In this subsection, we investigate how the profiles of the solution evolve in time. We will use the numerical results in Case 1 computed on the adaptive mesh of size $(n, m) = (1024, 512)$. We have computed the numerical solution in this case up to time $t = 1.76 \times 10^{-4}$ when it is still well resolved. We cannot guarantee the reliability of our computation in Case 1 beyond this time due to the loss of resolution, which will be discussed in Appendix C. The computation roughly consists of three phases: a warm-up phase ($t \in [0, 1.6 \times 10^{-4}]$), a stable phase ($t \in (1.6 \times 10^{-4}, 1.75 \times 10^{-4}]$), and a phase afterward ($t > 1.75 \times 10^{-4}$). In the warm-up phase, the solution evolves from the smooth initial data into a special structure. In the stable phase, the solution maintains a certain geometric structure and blows up stably. Beyond the stable phase, the solution starts to exhibit some unstable features that may arise from underresolution, and the tail part of the solution also generates some shearing induced oscillations that are hard to resolve. A study of the unstable behavior of the solution beyond the stable phase is presented in Appendix C in [HH22b].

Remark 3.1. To have a better understanding of the solution behavior during the time interval $[0, 1.76 \times 10^{-4}]$, we first discuss the characteristic time and length scales of our problem. Since the solution of the Euler equations with degenerate viscosity coefficients develops a potential focusing singularity, the characteristic length scale of the solution will decrease rapidly in time, and the maximal magnitude of the velocity will grow in time. For our initial data, the characteristic length scale is 10^{-4} and $\|\boldsymbol{u}\|_{L^\infty} \sim 10$, so the characteristic time scale is about $10^{-4}/\|\boldsymbol{u}\|_{L^\infty} \sim 10^{-5}$. At the time instant $t = 1.76 \times 10^{-4}$, the characteristic length scale drops to 10^{-6} and $\|\boldsymbol{u}\|_{L^\infty} \sim 50$, so the characteristic time scale is about $10^{-6}/\|\boldsymbol{u}\|_{L^\infty} \sim 2 \times 10^{-8}$. For the record, an extrapolation of our numerical fitting of the potentially singular solution implies that the potential blowup time is around 1.79×10^{-4}. Thus, 1.76×10^{-4} is quite close to the potential blowup time.

Figure 3.1 illustrates the evolution of u_1, ω_1 in the late warm-up phase by showing the solution profiles at three different times $t = 1.38 \times 10^{-4}, 1.55 \times 10^{-4}, 1.63 \times 10^{-4}$. We can see that the magnitudes of u_1, ω_1 grow in time. The "peak" parts of the profiles travel toward the symmetry axis $r = 0$ and shrink in space. The profile of u_1 develops sharp gradients around the peak; in particular, it develops a sharp front in

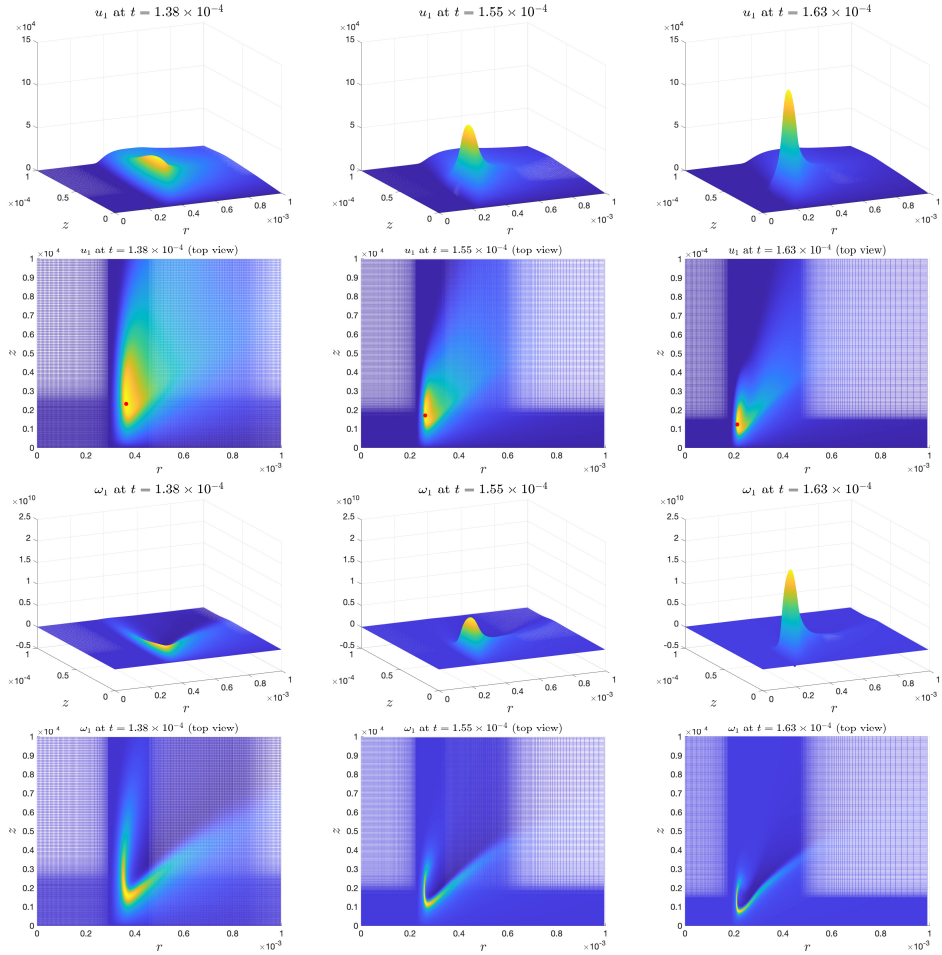

FIG 3.1. *The evolution of the profiles of* u_1 *(rows* 1 *and* 2*) and* ω_1 *(rows* 3 *and* 4*) in Case* 1. *Lines* 1 *and* 3 *are the profiles of* u_1, ω_1 *at three different times; lines* 2 *and* 4 *are the corresponding top views. The red dot is the location of the maximum point of* u_1.

the r direction. This is clearer if we look at the cross sections of u_1 in both directions (Figure 3.2). Moreover, ω_1 develops a thin curved structure. Between the sharp front and the symmetry axis $r = 0$, there is a no-spinning region where u_1, ω_1 are almost 0. On the outer side, both u_1 and ω_1 form a long tail part propagating toward the far field.

Let $(R(t), Z(t))$ denote the maximum point of $u_1(r, z, t)$. We will use this notation throughout the paper. Figure 3.2 shows the cross sections of u_1 going through the point $(R(t), Z(t))$ in both directions. That is, we plot $u_1(r, Z(t), t)$ versus r and $u_1(R(t), z, t)$ versus z, respectively. Again, it is clear that u_1 develops sharp gradients in both directions. In the r direction, u_1 forms a sharp front and a no-spinning region between the sharp front and $r = 0$. In the z direction, the profile of u_1 seems to develop a compact support that is shrinking toward $z = 0$.

3.2. Two scales. Figure 3.3 (first column) shows the trajectory of the maximum point $(R(t), Z(t))$ of $u_1(r, z, t)$. We can see that $(R(t), Z(t))$ moves toward the origin

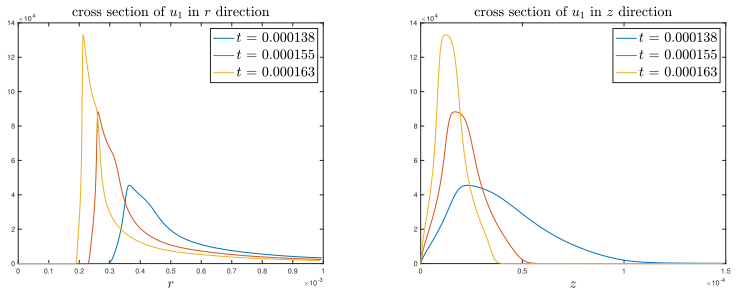

FIG 3.2. *Cross sections of u_1 in both directions at different times.*

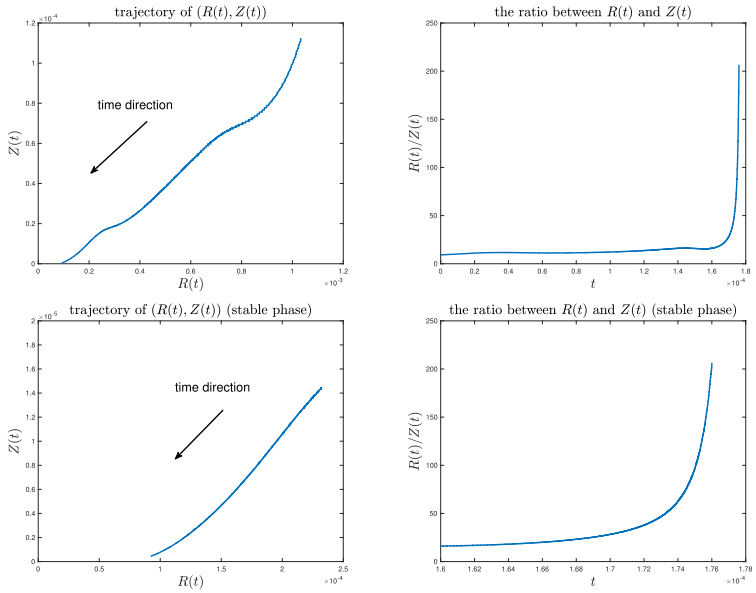

FIG 3.3. *The trajectory of $(R(t), Z(t))$ and the ratio $R(t)/Z(t)$ as a function of time for $t \in [0, 1.76 \times 10^{-4}]$. First row: the whole computation. Second row: the stable phase.*

$(r, z) = (0, 0)$, but with different rates in the two directions. This trajectory tends to become parallel to the horizontal axis $z = 0$ in the stable phase, which shows that $Z(t)$ approaches 0 much faster than $R(t)$. As shown in the second column of Figure 3.3, the ratio $R(t)/Z(t)$ grows rapidly in time, especially in the stable phase. This evidence implies that there are two separate spatial scales in the solution. We can see this more clearly if we plot the solution profiles in a square domain in the rz-plane. For example, Figure 3.4 shows the profiles and level sets of u_1, ω_1 at time $t = 1.63 \times 10^{-4}$ in a square domain $\{(r, z) : 0 \le r \le 10^{-3}, 0 \le z \le 10^{-3}\}$. The profiles have a sharp front in the r direction and are extremely thin in the z direction, which corresponds to the scale of $Z(t)$ (the smaller scale). The long spreading tails of the profiles and the distance between the sharp front and the symmetry axis $r = 0$ correspond to the scale of $R(t)$.

If we zoom in to a neighborhood of the smaller scale around the point $(R(t), Z(t))$, we can see that the smooth profiles of u_1, ω_1 are locally isotropic. Figure 3.5 shows the local isotropic profiles of u_1, ω_1 near the sharp front at a later time $t = 1.75 \times 10^{-4}$.

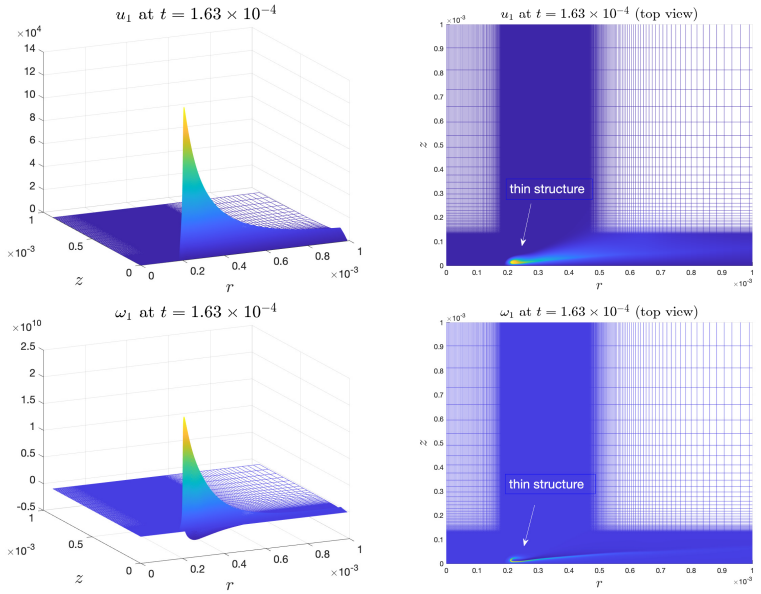

FIG 3.4. *Profiles and level sets of u_1 (first row) and ω_1 (second row) at time $t = 1.63 \times 10^{-4}$ in the square domain $\{(r,z) : 0 \le r \le 10^{-3}, 0 \le z \le 10^{-3}\}$.*

These profiles are very smooth with respect to the smaller scale. In fact, such local structures have been developed ever since the solution enters the stable phase ($t \ge 1.6 \times 10^{-4}$), and they remain stable afterward. We will further investigate this in section 6.5.

It is curious that the contours of u_1 and ω_1 seem to have the same shape. The thin structure of ω_1 behaves like a regularized 1D delta function supported along the "boundary" of the bulk part of u_1, which is roughly indicated by the red curve. In fact, we will see in section 6 that this phenomenon is evidence of the existence of a two-scale, locally self-similar blowup.

We remark that the numerical solutions computed in Case 3 have almost the same features as described above in Case 1. What varies most is how long these features can remain stable in time.

3.3. Rapid growth. The most important observation in our computation is the rapid growth of the solution. The maximums of $|u_1|, |\omega_1|$, and $|\boldsymbol{\omega}|$ as functions of time are reported in Figure 3.6. Here

$$\boldsymbol{\omega} = (\omega^\theta, \omega^r, \omega^z)^T = (r\omega_1\,,\, -ru_{1,z}\,,\, 2u_1 + ru_{1,r})^T$$

is the vorticity vector, and

$$|\boldsymbol{\omega}| = \sqrt{(\omega^\theta)^2 + (\omega^r)^2 + (\omega^z)^2}.$$

We can see that these variables grow rapidly in time. In particular, they grow rapidly in the stable phase ($t \in [1.6 \times 10^{-4}, 1.75 \times 10^{-4}]$). Moreover, the second row in Figure 3.6 shows that the solution grows much faster than a double-exponential rate.

The rapid growth of the maximum vorticity $\|\boldsymbol{\omega}\|_{L^\infty}$ is an important indicator of a finite-time singularity. In fact, the famous Beale–Kato–Majda criterion [BKM84]

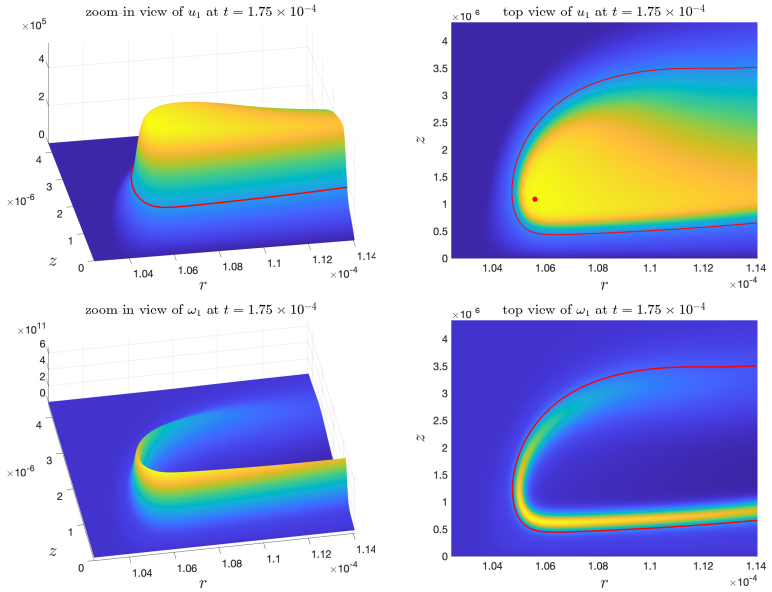

FIG 3.5. *Zoom-in views of* u_1, ω_1 *at time* $t = 1.75 \times 10^{-4}$. *First row: profile and top view of* u_1. *Second row: profile and top view of* ω_1. *The red curve (in all figures above) is the level set of* u_1 *for the value* $0.3\|u_1\|_{L^\infty}$, *and the red point is the maximum point of* u_1.

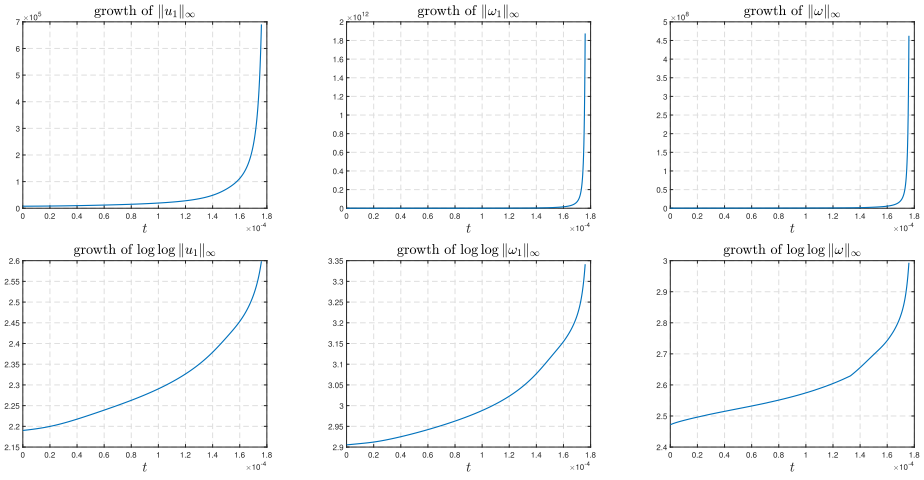

FIG 3.6. *First row: the growth of* $\|u_1\|_{L^\infty}$, $\|\omega_1\|_{L^\infty}$, *and* $\|\boldsymbol{\omega}\|_{L^\infty}$ *as functions of time. Second row:* $\log\log\|u_1\|_{L^\infty}$, $\log\log\|\omega_1\|_{L^\infty}$, *and* $\log\log\|\boldsymbol{\omega}\|_{L^\infty}$.

states that the solution to the standard Euler equations ceases to exist in some regularity class H^s (for $s \geq 3$) at some finite time T_* if and only if

$$\int_0^{T_*} \|\boldsymbol{\omega}(t)\|_{L^\infty} \mathrm{d}t = +\infty. \tag{3.1}$$

Although the Beale–Kato–Majda criterion does not apply to the case of degenerate viscosity coefficients directly, we can still use an argument similar to the H^s estimate of $\boldsymbol{u}$ in [BKM84] to show that the solution to the Euler equations (2.1) with

a degenerate viscosity coefficient ν ceases to exist in some regularity class H^s $(s \geq 3)$ if and only if

$$\int_0^{T_*} \|\nabla \boldsymbol{u}(t)\|_{L^\infty} \mathrm{d}t = +\infty.$$

Moreover, it is clear that $\|\boldsymbol{\omega}\|_{L^\infty} \lesssim \|\nabla \boldsymbol{u}\|_{L^\infty}$. Therefore, the rapid growth of maximum vorticity $\|\boldsymbol{\omega}\|_{L^\infty}$ is still a good indicator for a finite-time singularity even in the case of a degenerate viscosity coefficient. We thus still view $\|\boldsymbol{\omega}\|_{L^\infty}$ as a quantity of interest in our discussions. We will demonstrate in section 6 that the growth of $\|\boldsymbol{\omega}\|_{L^\infty}$ has a good fitting (with R^2 value greater that 0.9999) to an inverse power law

$$\|\boldsymbol{\omega}(t)\|_{L^\infty} \approx (T-t)^{-\gamma}$$

for some finite time T and some power $\gamma > 1$ (see section 6.2). This then implies that the solution shall develop a potential singularity at some finite time T.

3.4. Velocity field. In this subsection, we investigate the geometric structure of the velocity field. We first study the 3D velocity field $\boldsymbol{u} = u^r \boldsymbol{e}_r + u^\theta \boldsymbol{e}_\theta + u^z \boldsymbol{e}_z$ (denoted by (u^r, u^θ, u^z)) by looking at the induced streamlines. An induced streamline $\{\Phi(s; X_0)\}_{s \geq 0} \subset \mathbb{R}^3$ is completely determined by the background velocity $\boldsymbol{u}$ and the initial point $X_0 = (x_0, y_0, z_0)^T$ through the initial value problem

$$\frac{\partial}{\partial s}\Phi(s; X_0) = \boldsymbol{u}(\Phi(s; X_0)), \quad s \geq 0; \quad \Phi(0; X_0) = X_0.$$

We remark that the induced streamlines do not give the particle trajectories in the real computation; they only characterize the geometric structure of the velocity field $\boldsymbol{u}(t)$ for a fixed physical time t. The parameter s does not correspond to the physical time t.

We will generate different streamlines with different initial points $X_0 = (r_0 \cos(2\pi\theta), r_0 \sin(2\pi\theta), z_0)^T$. Since the velocity field $\boldsymbol{u}$ is now axisymmetric, the geometry of the streamline only depends on (r_0, z_0). Varying the angular parameter θ only demonstrates the rotational symmetry of the streamlines.

3.4.1. A tornado singularity. Figure 3.7 shows the streamlines induced by the velocity field $\boldsymbol{u}(t)$ at $t = 1.7 \times 10^{-4}$ in a macroscopic scale (the whole cylinder domain $\mathcal{D}_1 \times [0, 2\pi]$) for different initial points with (a) $(r_0, z_0) = (0.8, 0.01)$ and (b)

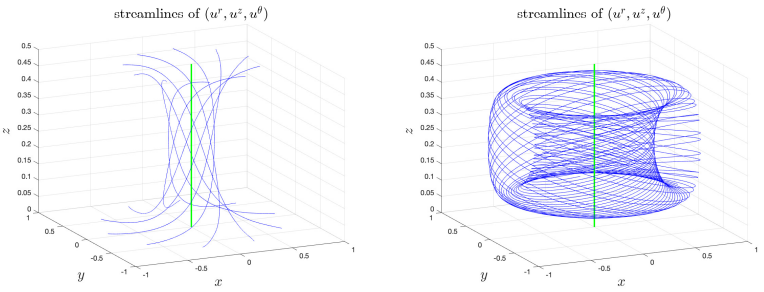

(a) $r_0 = 0.8$, $z_0 = 0.01$ **(b)** $r_0 = 0.8$, $z_0 = 0.1$

FIG 3.7. *The streamlines of* $(u^r(t), u^\theta(t), u^z(t))$ *at time* $t = 1.7 \times 10^{-4}$ *with initial points given by* (a) $(r_0, z_0) = (0.8, 0.01)$ *and* (b) $(r_0, z_0) = (0.8, 0.1)$. *The green pole is the symmetry axis* $r = 0$.

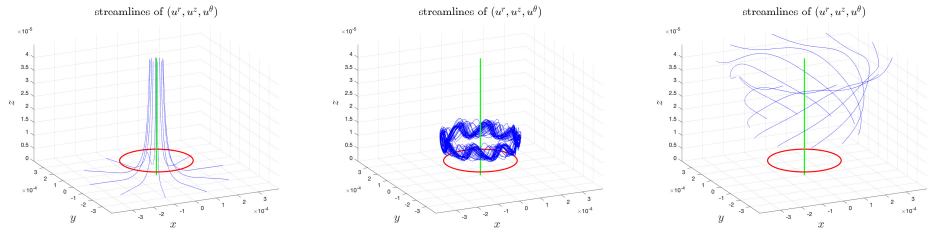

(a) $r_0 = 2R(t)$, $z_0 = 0.01Z(t)$ **(b)** $r_0 = 1.05R(t)$, $z_0 = 2Z(t)$ **(c)** $r_0 = 1.5R(t)$, $z_0 = 3Z(t)$

FIG 3.8. *The streamlines of* $(u^r(t), u^\theta(t), u^z(t))$ *at time* $t = 1.7 \times 10^{-4}$ *with initial points given by* (a) $(r_0, z_0) = (2R(t), 0.01Z(t))$, (b) $(r_0, z_0) = (1.05R(t), 2Z(t))$, *and* (c) $(r_0, z_0) = (1.5R(t), 3Z(t))$. $(R(t), Z(t))$ *is the maximum point of* $u_1(t)$, *indicated by the red ring. The green pole is the symmetry axis* $r = 0$.

$(r_0, z_0) = (0.8, 0.1)$. The velocity field resembles that of a tornado spinning around the symmetry axis (the green pole). If the streamline starts near the "ground" $(z = 0)$ as in Figure 3.7(a), it will first travel toward the symmetry axis, then move upward toward the "ceiling" $(z = 1/2)$, and at last turn outward away from the symmetry axis. In the meantime, it spins around the symmetry axis. On the other hand, if the initial point is higher (in the z coordinate) as in Figure 3.7(b), the streamline will not get very close to the symmetry axis. Instead, it will travel in an "inward-upward-outward-downward" cycle in the rz-coordinates and, in the meantime, circle around the symmetry axis.

Next, we take a closer look at the blowup region near the sharp front. Figure 3.8 shows the streamlines at time $t = 1.7 \times 10^{-4}$ for different initial points near the maximum point $(R(t), Z(t))$ of $u_1(t)$. The red ring represents the location of $(R(t), Z(t))$, and the green pole is the symmetry axis $r = 0$. The three settings of (r_0, z_0) are as follows.

(a) $(r_0, z_0) = (2R(t), 0.01Z(t))$. The streamline starts near the "ground" $z = 0$ and below the red ring $(R(t), Z(t))$. It first travels toward the symmetry axis and then travels upward away from $z = 0$. The spinning is weak since $u^\theta = ru_1$ is small in the corresponding region.

(b) $(r_0, z_0) = (1.05R(t), 2Z(t))$. The streamline starts right above the ring $(R(t), Z(t))$. It gets trapped in a local region, oscillating and spinning around the symmetry axis periodically. The spinning is strong.

(c) $(r_0, z_0) = (1.5R(t), 3Z(t))$. The streamline starts even higher and away from the ring $(R(t), Z(t))$. It spins upward and outward, traveling away from the blowup region.

3.4.2. The 2D flow. To understand the phenomena in the blowup region as shown in Figure 3.8, we look at the 2D velocity field (u^r, u^z) in the computational domain $\mathcal{D}_1$. Figure 3.9(a) shows the vector field of $(u^r(t), u^z(t))$ in a local microscopic domain $[0, R_b] \times [0, Z_b]$, where $R_b = 2.5R(t) \approx 3.97 \times 10^{-4}$ and $Z_b = 8Z(t) = 4.50 \times 10^{-5}$. The domain has been rescaled in the figure for better visualization. Figure 3.9(b) is a schematic for the vector field in Figure 3.9(a).

We can see that the streamline below $(R(t), Z(t))$ first travels toward $r = 0$ and then moves upward away from $z = 0$, bypassing the sharp front near $(R(t), Z(t))$, which again demonstrates the "two-phase" feature of the flow. As the flow gets close to $r = 0$, the strong axial velocity u^z transports u_1 from near $z = 0$ upward along the

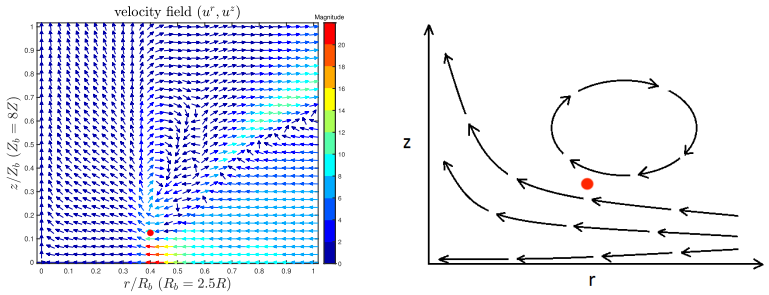

(a) the velocity field (u^r, u^z) **(b)** a schematic

FIG 3.9. (a) *The velocity field* $(u^r(t), u^z(t))$ *near the maximum point* $(R(t), Z(t))$ *of* $u_1(t)$ *(the red point) at* $t = 1.7 \times 10^{-4}$. *The color corresponds to the magnitude of* $\sqrt{(u^r)^2 + (u^z)^2}$. *The size of the domain has been rescaled.* (b) *A schematic of the vector field near the point* $(R(t), Z(t))$.

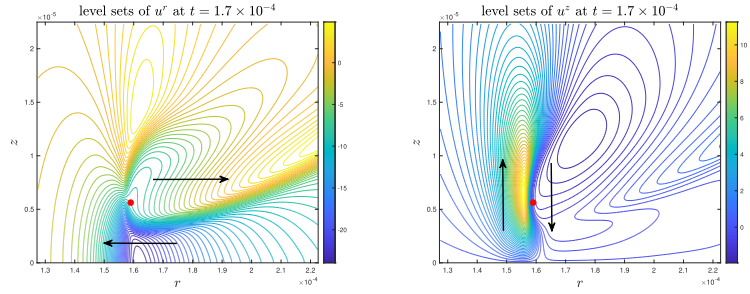

FIG 3.10. *The level sets of* u^r *(left) and* u^z *(right) at* $t = 1.7 \times 10^{-4}$. *The red point is the maximum point* $(R(t), Z(t))$ *of* $u_1(t)$.

z direction. Due to the odd symmetry of u_1, the angular velocity $u^\theta = ru^1$ is almost 0 in the region near $z = 0$. As a consequence, the upward stream dynamically generates a no-spinning region between the sharp front of u_1 and the symmetry axis $r = 0$. This no-spinning region resembles the calm eye of a tornado, an area of relatively low wind speed near the center of the vortex. This explains why the streamlines almost do not spin around the symmetry axis in this region, as illustrated in Figure 3.8(a).

Moreover, the velocity field $(u^r(t), u^z(t))$ forms a closed circle right above $(R(t), Z(t))$ as illustrated in Figure 3.9(b). The corresponding streamline is hence trapped in the circle region in the rz-plane. Since u_1 is large in this region (see Figure 3.5(a) and use the red point as a reference), the fluid spins fast around the symmetry axis $r = 0$. Consequently, the corresponding streamline travels fast inside a 3D torus surrounding the symmetry axis. This explains the oscillating and circling in Figure 3.8(b). This local circle structure of the 2D velocity field is critical in stabilizing the blowup process, as it keeps the major profiles of u_1, ω_1 traveling toward the origin instead of being pushed upward.

The velocity field $(u^r(t), u^z(t))$ can also explain the sharp structures of u_1, ω_1 in their local profiles (as shown in Figure 3.5(a), (b)). Figure 3.10 shows the level sets of u^r, u^z at $t = 1.7 \times 10^{-4}$. One can see that the radial velocity u^r has a strong shearing layer below $(R(t), Z(t))$ (the red point). This shearing contributes to the sharp gradient of u_1 in the z direction (e.g., see Figure 3.5(a)). Similarly, the axial

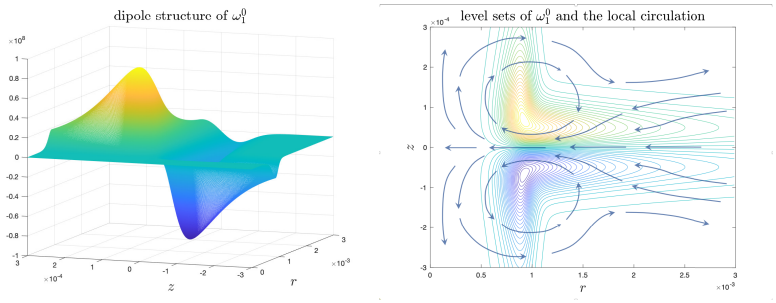

FIG 3.11. *The dipole structure of the initial data ω_1^0 and the induced local velocity field.*

velocity u^z also has a strong shearing layer close to the point $(R(t), Z(t))$. This shearing explains the sharp front of u_1 in the r direction. We will also explain in section 6.6 the formation of a sharp front in the r direction from a different perspective.

3.5. Understanding the blowup mechanism. In this subsection, we elaborate our understanding of the potential blowup by examining several critical factors that lead to a sustainable blowup solution.

3.5.1. Vortex dipole and hyperbolic flow. Though we have only shown numerical results in the half-period domain $\mathcal{D}_1 = \{(r,z); 0 \le r \le 1, 0 \le z \le 1/2\}$, one should keep in mind that the real meaningful physics happens in the whole period $\{(r,z); 0 \le r \le 1, -1/2 \le z \le 1/2\}$. Moreover, the 2D velocity field (u^r, u^θ) can be extended to the negative r-plane as an even function of r. The odd symmetry (in z) of the initial data of ω_1 leads to a dipole structure of the angular vorticity ω^θ, which then induces a hyperbolic flow in the rz-plane with a pair of antisymmetric (with respect to z) local circulations. This pair of antisymmetric convective circulations is the cornerstone of our blowup scenario, as it has the desirable property of pushing the solution near $z = 0$ toward $r = 0$.

Figure 3.11 presents the dipole structure of the initial data ω_1^0 in a local symmetric region $(r,z) \in [0, 3\times 10^{-3}] \times [-3\times 10^{-4}, 3\times 10^{-4}]$ and the hyperbolic velocity field induced by it. The negative radial velocity near $z = 0$ induced by the antisymmetric vortex dipole pushes the solution toward $r = 0$, which is one of the driving mechanisms for a singularity on the symmetry axis. However, we also need another mechanism that squeezes the solution toward $z = 0$, so that it can be driven by the inward velocity. Otherwise, the upward velocity away from $z = 0$ may destroy the blowup trend. This critical squeezing mechanism comes from the odd symmetry of u_1.

3.5.2. The odd symmetry and sharp gradient of u_1. The odd symmetry of u_1 is not required for ω_1 to be odd at $z = 0$. The reason we construct u_1 to be an odd function of z is that it ensures that u_1^2 has a large gradient in the z direction near $z = 0$.

It is clear from the ω_1 equation (2.2b) that the driving force for ω_1 to blow up is the vortex stretching term $2(u_1^2)_z$. The odd symmetry of u_1 ensures that $u_1(r, 0, t) = 0$ for all $t \ge 0$. Therefore, $(u_1^2)_z$ is positive and large somewhere between $z = Z(t)$ and $z = 0$, which drives ω_1 to grow fast near $z = 0$. The growth of ω_1 then feeds the growth of u^r (in absolute value) around $z = 0$, as a stronger dipole structure of the angular vorticity ω^θ induces a stronger inward flow in between the dipole (as demonstrated in Figure 3.11). Note that u^r being negative means $\psi_{1,z} = -u^r/r$ is positive, and the growth of u^r around $z = 0$ implies the growth of $\psi_{1,z}$ there, especially near $r = R(t)$.

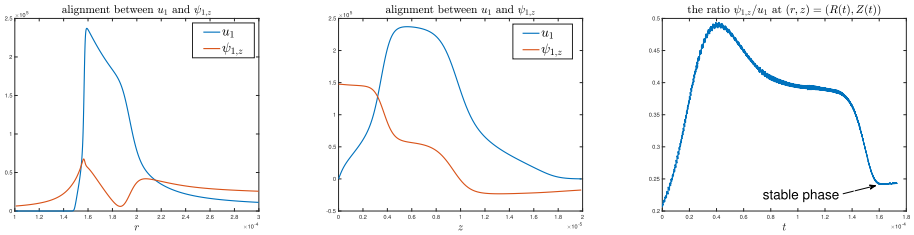

(a) r cross sections of $u_1, \psi_{1,z}$ **(b)** z cross sections of $u_1, \psi_{1,z}$ **(c)** $\psi_{1,z}/u_1$ as a function of time

FIG 3.12. *The alignment between* u_1 *and* $\psi_{1,z}$. (a) *and* (b) *Cross sections of* u_1 *and* $\psi_{1,z}$ *through the point* $(R(t), Z(t))$ *at* $t = 1.7 \times 10^{-4}$. (c) *The ratio* $\psi_{1,z}/u_1$ *at the point* $(R(t), Z(t))$ *as a function of time up to* $t = 1.75 \times 10^{-4}$.

This in turn contributes to the rapid growth of u_1 in the critical region near $z = 0$ through the vortex stretching term $2\psi_{1,z}u_1$ in the u_1 equation (2.2a).

Moreover, since $\psi_1 = 0$ along $z = 0$ (by the odd condition), the Poisson equation (2.2c) can be approximated by $\psi_{1,zz} \approx -\omega_1$ near $z = 0$. This means that $\psi_{1,z}$, as a function of z, achieves its local maximum at $z = 0$ in a neighborhood where $\text{sign}(\omega_1) = \text{sign}(z)$. The rapid growth of $\psi_{1,z}$ and the nonlinear vortex stretching term $2\psi_{1,z}u_1$ in the u_1 equation induce a traveling wave for u_1 propagating toward $z = 0$, which drags the maximum point of u_1 toward $z = 0$. The traveling wave is so strong that it overcomes the stabilizing effect of advection along the z direction, which pushes the flow upward away from $z = 0$. The fact that the maximum point of u_1 traveling toward $z = 0$ generates an even sharper gradient of u_1^2 in the z direction. The whole coupling mechanism above forms a positive feedback loop,

$$(u_1^2)_z \uparrow \implies \omega_1 \uparrow \implies \psi_{1,z} \uparrow \implies u_1 \uparrow \implies (u_1^2)_z \uparrow, \tag{3.2}$$

that leads to a sustainable blowup solution shrinking toward $z = 0$ and traveling toward $r = 0$.

To trigger this mechanism, it is important that the initial data have the proper symmetry and a strong alignment between u_1 and ω_1 as described in Appendix A.1. The maximum point of ω_1 should align with the location where $u_{1,z}$ is positive and large, which is slightly lower (in z) than the maximum point of u_1. This is one of the guiding principles in the construction of our initial data.

Figure 3.12 demonstrates the alignment between $\psi_{1,z}$ and u_1. Figure 3.12(b) shows the cross section of $u_1, \psi_{1,z}$ in the z direction through $(R(t), Z(t))$ at $t = 1.7 \times 10^{-4}$. We can see that $\psi_{1,z}(R(t), z, t)$ is monotonically decreasing for $z \in [0, 2Z(t)]$ and relatively flat for $z \in [0, 0.5Z(t)]$. Moreover, $\psi_{1,z}$ is large, positive, and comparable to u_1 in magnitude, which leads to the rapid growth of u_1 and pushes $Z(t)$ moving toward $z = 0$. Figure 3.12(c) shows the alignment ratio $\psi_{1,z}(R(t), Z(t), t)/u_1(R(t), Z(t), t)$, i.e., the alignment between $\psi_{1,z}$ and u_1 at the maximum point of u_1. One can see that the ratio $\psi_{1,z}/u_1$ settles down to a stable value at $(R(t), Z(t))$ in the stable phase which is characterized by the time interval $[1.6 \times 10^{-4}, 1.75 \times 10^{-4}]$; that is, $\psi_{1,z}(R(t), Z(t), t) \sim u_1(R(t), Z(t), t)$ in the stable phase. Consequently, the vortex stretching term in the u_1 equation is formally quadratic at the maximum point of u_1 if we ignore the small viscosity,

$$\frac{\mathrm{d}}{\mathrm{d}t} u_{1,\max} \approx u_{1,\max}^2 ,$$

which implies that maximum u_1 should blow up like $(T-t)^{-1}$ for some finite time T. We will see this observation more clearly in section 6.

We remark that the above discussion on the potential blowup mechanism also applies to the 3D axisymmetric Euler equations in the same scenario. We therefore expect that the solution to the Euler equations (in Case 3) would develop a similar blowup if we were able to resolve the small scale features of the solution.

4. Comparison with the original Navier–Stokes equations. In this section, we compare the solution to the equations (2.2) with the variable viscosity coefficients (A.3) (Case 1) and the solution to the original Navier–Stokes equations (Case 2) using the same initial-boundary conditions (2.4) and (A.1). This comparison will explain why the degeneracy of the variable viscosity coefficients is crucial for the solution to develop a potential finite-time singularity. In fact, we observe that the Navier–Stokes equations with a constant viscosity coefficient will destroy the critical two-scale feature of the solution and eventually prevent the finite-time blowup.

4.1. Profile evolution in Case 2. In section 3, we studied the evolution of the solution in Case 1 and observed a stable blowup with a two-scale feature. Here, we investigate how the solution evolves differently when the degenerate viscosity coefficients ν^r, ν^z are replaced by a constant μ. As an illustration, we will focus our study on the case where $\mu = 10^{-5}$. In what follows, Case 2 refers to the computation of the Navier–Stokes equations with constant viscosity coefficient $\mu = 10^{-5}$ without further clarification. Similar phenomena have been observed in Case 2 when μ takes different values.

Figure 4.1 demonstrates the evolution of the solution in Case 2 from $t = 1.6\times 10^{-4}$ to $t = 2 \times 10^{-4}$. One should notice the obvious difference in behavior between the solution in Case 1 and that in Case 2 when comparing Figures 4.1 with 3.1. Below we list some of our observations.

- Unlike in Case 1, the computation in Case 2 can be continued to a much later time, and the solution still remains quite smooth.
- The solution does not change much from $t = 1.6 \times 10^{-4}$ to $t = 2 \times 10^{-4}$. In particular, it does not develop a two-scale spatial structure. Instead, it maintains a profile with a single scale that is comparable to $R(t)$, the distance between the maximum point of u_1 and the symmetry axis $r = 0$. Moreover, the profile of u_1 does not form a sharp gradient in the z direction or a sharp front in the r direction, and the profile of ω_1 does not develop a thin structure.
- The maximums of the solution u_1 and ω_1 only grow modestly in the early stage and eventually decrease in the late stage. From $t = 0$ to $t = 2 \times 10^{-4}$, $\|u_1\|_{L^\infty}$ increases only by a factor of 2.34, and $\|\omega_1\|_{L^\infty}$ increases only by a factor of 3.67.

These observations suggest that the solution in Case 2 does not develop a finite-time blowup, at least not in the same way as in Case 1. The main reason for such a difference in behavior is that the viscosity term with a constant viscosity coefficient is so strong that it regularizes the smaller scale $Z(t)$ in the two-scale solution profile that we observed in section 3.5 and thus destroys the critical blowup mechanism. We will explain in section 6.6 why the degenerate viscosity coefficient is crucial for a two-scale blowup to appear and persist.

Figure 4.2 compares the trajectories of $(R(t), Z(t))$ and the ratios $R(t)/Z(t)$ in Case 1 for $t \in [0, 1.76 \times 10^{-4}]$ and in Case 2 for $t \in [0, 3 \times 10^{-4}]$. We can see that, due to the effect of the stronger viscosity, the point $(R(t), Z(t))$ in Case 2 does not travel toward the symmetry axis $r = 0$ or toward the symmetry plane $z = 0$ as fast as

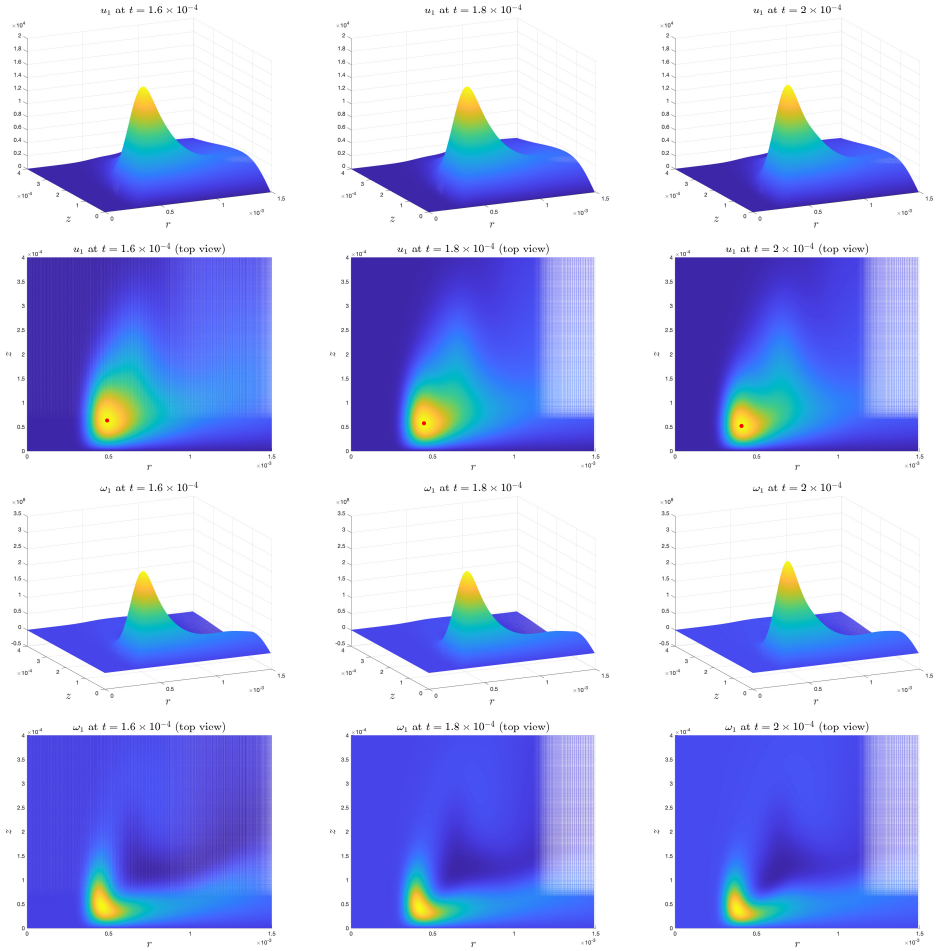

FIG 4.1. *The evolution of the profiles of* u_1 *(rows* 1 *and* 2*) and* ω_1 *(rows* 3 *and* 4*) in Case* 2 *with* $\nu^r = \nu^z = 10^{-5}$. *Lines* 1 *and* 3 *are the profiles of* u_1, ω_1 *at three different times; lines* 2 *and* 4 *are the corresponding top views. The red dot is the location of the maximum point of* u_1.

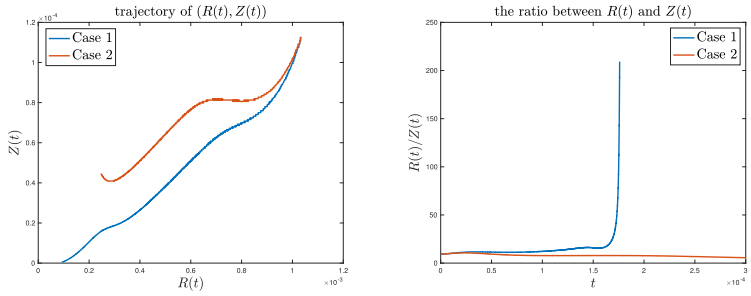

FIG 4.2. *Left: trajectories of* $(R(t), Z(t))$ *in Case* 1 *and in Case* 2. *Right: ratios between* $R(t), Z(t)$ *in Case* 1 *and in Case* 2. *Blue curves: Case* 1 *for* $t \in [0, 1.76 \times 10^{-4}]$. *Red curves: Case* 2 *for* $t \in [0, 3 \times 10^{-4}]$.

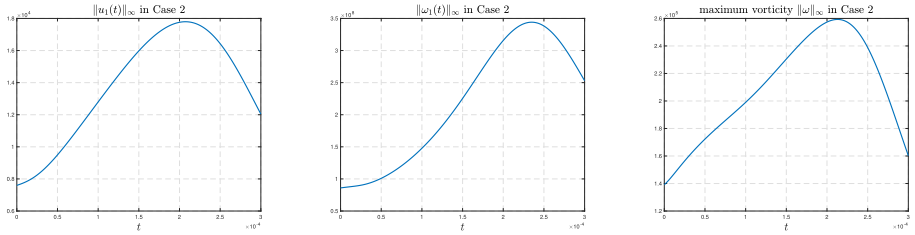

FIG 4.3. *The values of* $\|u_1\|_{L^\infty}$, $\|\omega_1\|_{L^\infty}$, *and* $\|\boldsymbol{\omega}\|_{L^\infty}$ *as functions of time in Case* 2.

in Case 1. The ratio $R(t)/Z(t)$ in Case 2 does not increase rapidly; instead, the two coordinates remain comparable to each other. This again confirms that the solution does not develop the critical two-scale feature in Case 2. More interestingly, the red trajectory turns upward after some time, suggesting that there will be no blowup focusing at the origin $(r, z) = (0, 0)$ in Case 2. This is consistent with our discussion in section 3.5 that when there is no two-scale feature, the main profile of the solution will eventually be pushed away from the "ground" $z = 0$ by the upward flow. As a result, the critical blowup mechanism in our scenario will be destroyed.

4.2. Growth of some key quantities in Case 2. To further illustrate that the solution will remain regular in Case 2, we directly study the growth of different solution variables. Figure 4.3 plots the maximums of $u_1, \omega_1, |\boldsymbol{\omega}|$ as functions of time. We can see that these quantities do not increase rapidly as in Case 1 (compared to the dramatic growth shown in Figure 3.6); moreover, they all start to decrease after some time. Note that the Beale–Kato–Majda criterion (see section 3.3) also applies to the Navier–Stokes equations: the solution develops a singularity at some finite time T if and only if $\int_0^T \|\boldsymbol{\omega}\|_{L^\infty} \mathrm{d}t = +\infty$. From Figure 4.3 we can see that the maximum vorticity $\|\boldsymbol{\omega}\|_{L^\infty}$ tends to remain bounded, at least for the duration of our computation. This observation strongly suggests that the solution to the equations (2.2) with a constant viscosity coefficient (namely the Navier–Stokes equations) will not blow up under the initial-boundary conditions (2.4), (A.1).

To understand why the maximum of u_1 does not rise rapidly and eventually drops in the later stage in Case 2, we study the competition between the vortex stretching and the viscosity. Since $2u_1$ is the leading order part of the axial vorticity $\omega^z = 2u_1 + ru^r$ for r near 0, the forcing term $2\psi_{1,z}u_1$ in the u_1 equation (2.2) can be considered as a vortex stretching term. This term is the driving force for the growth of u_1. On the contrary, the viscosity term f_{u_1} (given by (2.3a)), which is always negative at $(R(t), Z(t))$, damps the maximum of u_1. If the vortex stretching dominates the viscosity near $(R(t), Z(t))$, $\|u_1\|_{L^\infty}$ should grow; otherwise, $\|u_1\|_{L^\infty}$ will drop.

In Figure 4.4 we plot the relative magnitudes of the vortex stretching $2\psi_{1,z}$ and the viscosity $|f_{u_1}|/u_1$ at $(R(t), Z(t))$ in Case 1 (left) and in Case 2 (right). It is clear that the vortex stretching keeps growing and always dominates the viscosity term in the u_1 equations at $(R(t), Z(t))$ in Case 1; thus we observe a rapid growth of $\|u_1\|_{L^\infty}$ in time. This is the consequence of (i) the good alignment between $\psi_{1,z}$ and u_1 that relies on the thin structure (the smaller scale) of the solution in the z direction as described in section 3.5 and (ii) the fact that the viscosity coefficients are degenerate at the origin. On the contrary, we observe in Case 2 that the relative strength of the vortex stretching starts to decrease after some time and is dominated by the viscosity term in later time, which leads to the decrease of $\|u_1\|_{L^\infty}$. This is caused by the

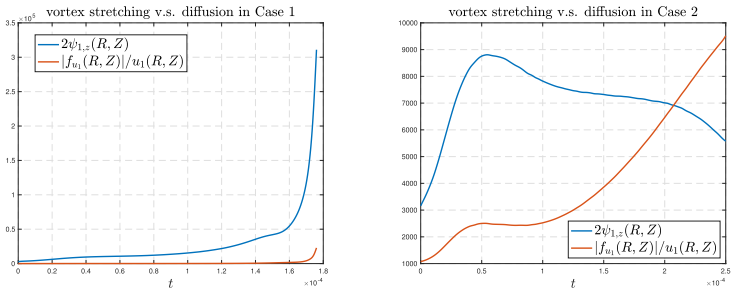

FIG 4.4. *The relative magnitudes of the vortex stretching* $2\psi_{1,z}$ *and the viscosity* $|f_{u_1}|/u_1$ *at the point* $(R(t), Z(t))$ *in Case* 1 *(left) and in Case* 2 *(right).*

strong viscosity from two aspects. On the one hand, if the blowup mechanism in section 3.5 tries to generate a thinner scale in the solution, then the viscosity with a constant/nondegenerate coefficient will become too strong for the smaller scale to survive, and thus the alignment between $\psi_{1,z}$ and u_1 is not sustainable. On the other hand, if the solution does not develop a two-scale structure, $\psi_{1,z}$ and u_1 cannot cannot develop a strong alignment for the coupling mechanism (3.2) to last. This dilemma prevents a sustainable blowup from occurring in Case 2.

We remark that we have carried out computations in Case 2 with different values of μ in the range $[10^{-7}, 10^{-4}]$, and we have made qualitatively similar observations in all trials: there is no sign of finite-time blowup for all tested values of μ. For a smaller μ, the solution in Case 2 in the early stage of the computation is very similar to the solution in Case 1, and a two-scale feature seems to develop. However, the viscosity with a constant coefficient will eventually take dominance and eliminate the potential two-scale blowup, and the maximum vorticity starts to drop afterward. If μ is even smaller ($\mu < 10^{-7}$), the viscosity term will be too weak to regularize the sharp fronts in the early stage of the computation and cannot effectively control the mild instability in the intermediate field and the far field where the mesh is not as dense as in the near field. The solution quickly becomes underresolved. It is still unclear whether the solution to the original 3D axisymmetric Navier–Stokes equations can develop a focusing blowup at the symmetry axis in a different manner when μ is sufficiently small. Yet we conjecture that this cannot happen in the two-scale manner described in Case 1.

5. Comparison with the Euler equations. In this section, we will discuss our potential blowup scenario in Case 3 of the Euler setting. That is, we study the evolution of the solution to the initial-boundary value problem (2.2)–(2.4) and (A.1) with $\nu^r = \nu^z = 0$. As an overview, the Euler solution behaves very similarly to the solution in our main Case 1 in the warm-up phase. This is not surprising as the critical blowup mechanism discussed in section 3.5 relies only on the Euler part of the equations. In particular, the Euler solution grows faster than the solution in Case 1 (with degenerate viscosity coefficients) during the warm-up phase. However, the Euler solution also quickly develops unfavorable oscillations in the critical blowup region, which is likely due to underresolution of the extremely sharp structure in the profile.

5.1. Profile evolution. To demonstrate that the solutions in Case 1 and Case 3 behave similarly in the warm-up phase, we compare their profiles at the same time instant. In Figure 5.1, we plot the profiles of u_1 and ω_1 at $t = 1.5 \times 10^{-4}$ in Case 1

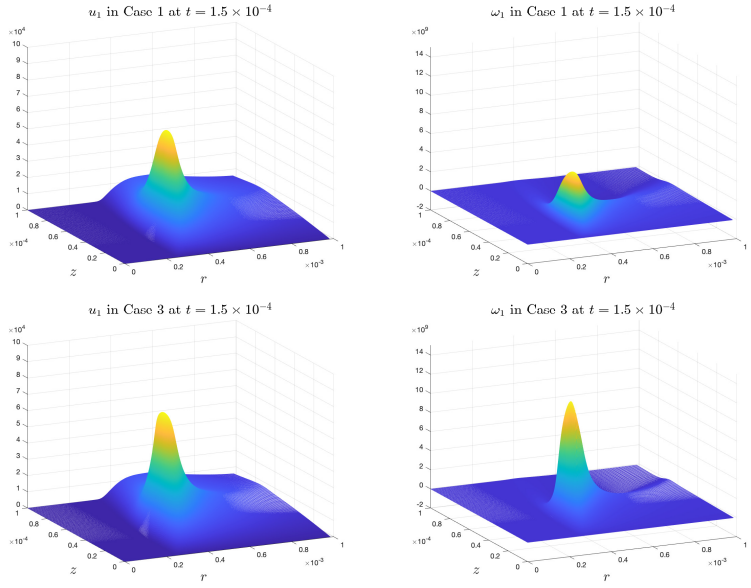

FIG 5.1. *The profiles of* u_1 *and* ω_1 *at* $t = 1.5 \times 10^{-4}$ *in Case* 1 *(first row) and in Case* 3 *(second row).*

(first row) and Case 3 (second row), respectively. We can see that the solution profiles in both cases are qualitatively similar, except that the solution in Case 3 grows faster. The solution also develops a sharp front in the r direction and a no-spinning region between the front and the symmetry axis $r = 0$.

As in Case 1, the solution in Case 3 also demonstrates two-scale features: a long tail in the r direction and a thin structure in the z direction. If we zoom in to the front part of the solution, we can also see local isotropic profiles that are similar to those in Case 1. Figure 5.2 compares the local profiles of ω_1 near the front part in Case 1 with those in Case 3 at $t = 1.55 \times 10^{-4}$. Again, these profiles are qualitatively similar. However, one can see that the ω_1 profile in Case 3 is much thinner at this early time, due to the absence of the regularization of the degenerate viscosity. Recall that, in Case 1, the curved structure of ω_1 only becomes very thin at a much later time (see Figure 3.5).

5.2. Even faster growth. Without the viscosity regularization, the solution in Case 3 grows even faster than that in Case 1. In Figure 5.3, we compare the growth of $\|u_1\|_{L^\infty}$, $\|\omega_1\|_{L^\infty}$, and $\|\boldsymbol{\omega}\|_{L^\infty}$ (in double-log scale) in Case 1 and Case 3. The plots stop at 1.6×10^{-4} when the solution in Case 3 is still resolved. We can see that these variables computed in Case 3 grow faster than a double-exponential rate, even above the corresponding growth curve in Case 3. This result implies that the solution in Case 1 may also develop a similar blowup at a finite time in a fashion similar to that of Case 3.

In fact, the Euler solution in Case 3 also enjoys the critical blowup mechanism discussed in section 3.5, which does not rely on the viscosity terms. Intuitively, the viscosity terms should slow down the blowup instead of promoting it. From this point of view, the Euler solution is more likely to blow up at a finite time.

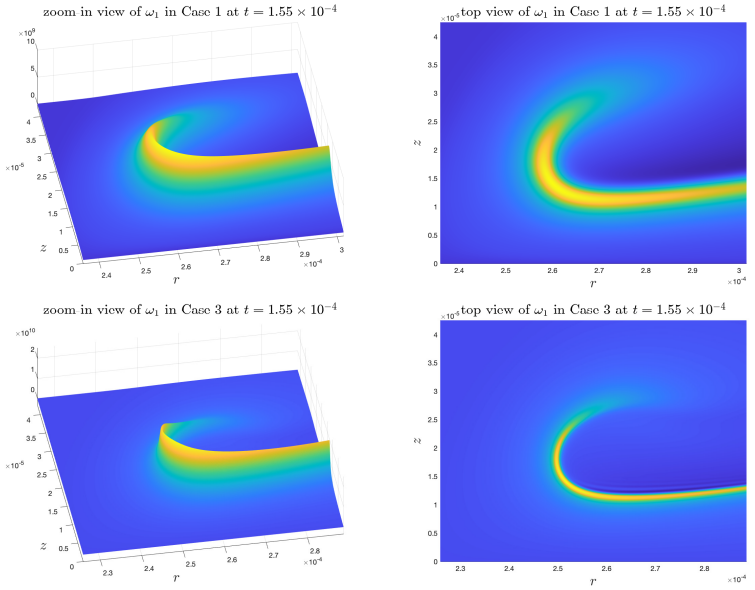

FIG 5.2. *The zoom-in profile and the top view of* ω_1 *at* $t = 1.55 \times 10^{-4}$ *in Case* 1 *(first row) and in Case* 3 *(second row).*

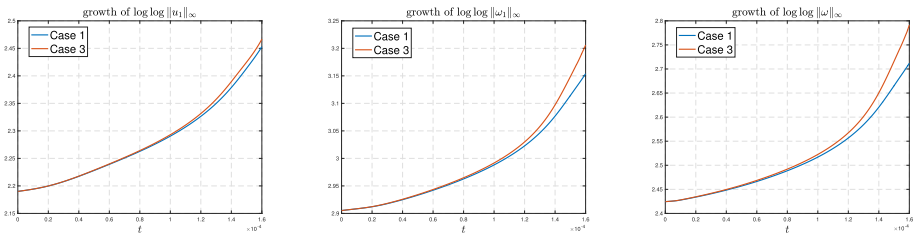

FIG 5.3. *Comparison between the growth of* $\|u_1\|_{L^\infty}$, $\|\omega_1\|_{L^\infty}$, *and* $\|\boldsymbol{\omega}\|_{L^\infty}$ *in Case* 1 *and Case* 3.

5.3. Underresolution at early time. Currently, we are not able to study thoroughly the potential blowup of the Euler solution in Case 3 for a longer time because the solution quickly develops visible oscillations in the critical region when it enters the stable phase (beyond $t = 1.6 \times 10^{-4}$). Figure 5.4 shows the top views of the profiles of u_1 and ω_1 in Case 3 at $t = 1.63 \times 10^{-4}$, computed with $(n, m) = (1024, 512)$ (first row) and $(n, m) = (2048, 1024)$ (second row), respectively. One can see that the oscillations appear not only in the tail part but also in the front part of the solution, which may disturb the crucial alignment between u_1 and $\psi_{1,z}$ near the maximum point of u_1. In fact, the oscillations already start to occur at an earlier time $t = 1.61 \times 10^{-4}$. Increasing the resolution can help suppress the oscillations (the plots in the second row of Figure 5.4 are less oscillatory than those in the first row), which implies that this phenomenon is a consequence of underresolution of the Euler solution. However, even if we use a finer mesh, the oscillations still appear quickly before we can obtain convincing numerical evidence of locally self-similar blowup at a finite time.

In Figure 5.5(a) and (b), we plot the cross sections of u_1 and $\psi_{1,z}$ through the point $(R(t), Z(t))$ at $t = 1.63 \times 10^{-4}$ in Case 3. We can see that the Euler solution

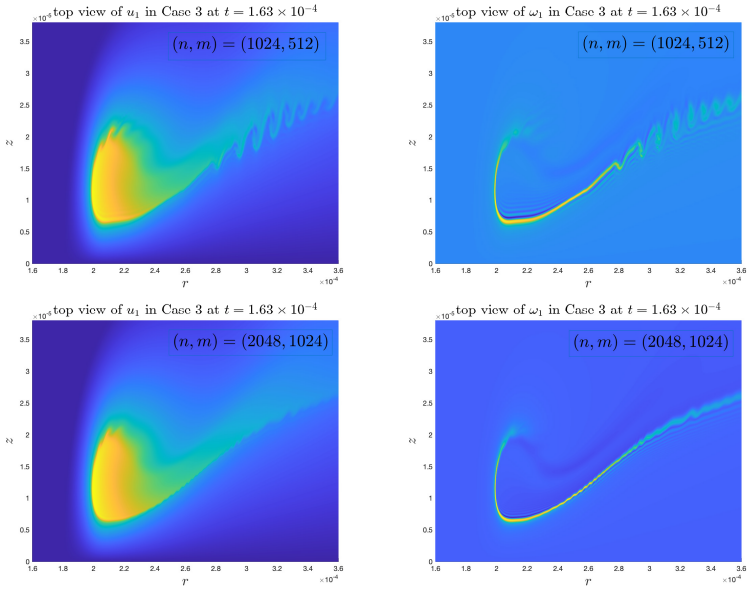

FIG 5.4. *Top views of the profiles of* u_1 *and* ω_1 *in Case* 3 *at* 1.63×10^{-4}*, computed with different resolutions. First row:* $(n, m) = (1024, 512)$*; second row:* $(n, m) = (2048, 1024)$*. Oscillations appear all over the profiles before the stable phase can last for a long time.*

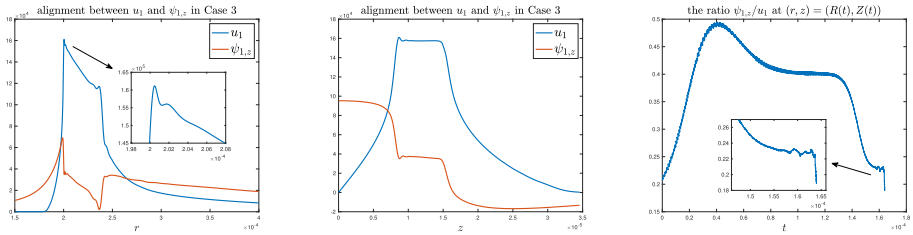

(a) r cross sections of $u_1, \psi_{1,z}$ **(b)** z cross sections of $u_1, \psi_{1,z}$ **(c)** $\psi_{1,z}/u_1$ as a function of time

FIG 5.5. *The alignment between* u_1 *and* $\psi_{1,z}$*.* (a) *and* (b) *Cross sections of* u_1 *and* $\psi_{1,z}$ *through the point* $(R(t), Z(t))$ *at* $t = 1.63 \times 10^{-4}$*.* (c) *The ratio* $\psi_{1,z}/u_1$ *at the point* $(R(t), Z(t))$ *as a function of time up to* $t = 1.64 \times 10^{-4}$*.*

also enjoys the favorable nonlinear alignment between u_1 and $\psi 1, z$ near the maximum point of u_1 as described in section 3.5. One should compare these plots with those in Figure 3.12. However, the underresolution of the Euler solution leads to oscillations in the front part of the u_1 profile, which may compromise the critical blowup mechanism. In Figure 5.5(c), we plot the ratio $\psi_{1,z}/u_1$ at $(R(t), Z(t))$ against time. The alignment between u_1 and $\psi_{1,z}$ begins to decrease before 1.64×10^{-4} due to underresolution.

A possible reason for the Euler solution to become underresolved at an early time is that the local geometric structure of the solution becomes too singular to be resolved by our current adaptive mesh strategy. The front of u_1 is much sharper and the structure of ω_1 is much thinner than that in Case 3 at the same time instant. If we treat the thickness of the thin structure of ω_1, denoted by $d(t)$, as an additional spatial scale, then this scale is even smaller than the scale of $Z(t)$. That is, the Euler solution demonstrates three separate spatial scales $d(t), Z(t), R(t)$ (from small

to large), each converging to 0 at a different rate. However, our adaptive mesh strategy is only powerful enough to handle the high contrast between two separate scales in the critical region of the solution over the stable phase. The three-scale feature of the Euler solution in Case 3 is beyond our current computational capacity. Moreover, the thin 1D-like structure of ω_1 induces strong shearing instabilities that will amplify the errors from underresolution and lead to the visible rolling oscillations.

In summary, the Euler solution in Case 3 quickly develops an even more singular structure that is extremely difficult to resolve with our current computational capacity. This is why we adopt the degenerate viscosity coefficients in our main Case 1: the degenerate viscosity is strong enough to prevent the occurrence of a third scale but also not too strong to suppress the two-scale blowup. We believe that the Euler solution may develop a locally self-similar blowup as in Case 1. To obtain convincing numerical evidence of a potential 3D Euler blowup, we need to develop a more effective adaptive mesh strategy and have access to larger computational resources. We will leave this to our future work.

6. Potential blowup scaling analysis. In this section, we will quantitatively examine the features of the potential blowup in our computation. We will first provide adequate numerical evidence that the growth and the spatial scaling of the solution obey some (inverse) power laws, which suggests that a finite-time singularity exists in a locally self-similar form. In particular, we employ a linear fitting procedure to estimate the blowup rates and scalings. Then we will perform an asymptotic analysis of the potential blowup based on a two-scale self-similar ansatz. We show that the results of the asymptotic analysis are highly consistent with our numerical results, supporting the existence of a locally self-similar blowup.

6.1. Linear fitting procedure. The most straightforward way to numerically identify a finite-time blowup is to study the growth rate of the solution. For a solution quantity $v(t)$ that is expected to blow up at some finite time T, a typical asymptotic model is the inverse power law:

$$v(t) \sim \alpha (T-t)^{-c_v} \quad \text{as} \quad t \to T, \tag{6.1}$$

where $c_v > 0$ is the blowup rate and $\alpha > 0$ is some constant. To verify that $v(t)$ satisfies an inverse power law and to learn the power c_v, we follow the idea of Luo and Hou [LH14b] and study the time derivative of the logarithm:

$$\frac{\mathrm{d}}{\mathrm{d}t} \log v(t) = \frac{v'(t)}{v(t)} \sim \frac{c_v}{T-t}.$$

This naturally leads to the linear regression model

$$y(t; v) := \frac{v(t)}{v'(t)} \sim -\frac{1}{c_v}(t-T) =: \tilde{a}t + \tilde{b} \tag{6.2}$$

with response variable y, explanatory variable t, and model parameters $\tilde{a} = -1/c_v, \tilde{b} = T/c_v$. Then the blowup rate c_v can be estimated via a standard least-squares procedure. The quality of the fitting using this model can be measured by the coefficient of determination (the R^2),

$$R^2 = 1 - \frac{SS_{\mathrm{err}}}{SS_{\mathrm{tot}}}$$

with a value close to 1 indicating a high quality fitting. Here $SS_{\mathrm{tot}} = \sum_i (y_i - \bar{y})^2$ is the total sum of squares, $SS_{\mathrm{err}} = \sum_i (y_i - \hat{y}_i)^2$ is the residual sum of squares, $y_i, \hat{y}_i$

denote the observed and predicted values of the response variable y, respectively, and $\bar{y}$ denotes the mean of the observed data y_i.

To have a convincing estimate of the blowup rate c_v, it is important that the fitting procedure is performed in a proper time interval $[t_1, t_2]$. First of all, this time interval must lie in the asymptotic regime of the inverse power law (6.1) if such scaling does exist. Second, the solution must be well resolved in this time interval $[t_1, t_2]$. As we have observed, the blowup settles down to a stable phase at around $t = 1.6 \times 10^{-4}$, after which the evolution of the solution begins to have a stable pattern. It is likely that the solution enters the asymptotic regime of the blowup after this time instant. In addition, we have learned in Appendix C that the numerical solution is resolved before $t = 1.76 \times 10^{-4}$. Therefore, according to the two criteria, we should place the fitting interval $[t_1, t_2]$ within the time interval $[1.6 \times 10^{-4}, 1.76^{-4}]$. Moreover, the interval should not to be too short; otherwise, any curve may look like a straight line. In particular, we choose $[t_1, t_2] = [1.60 \times 10^{-4}, 1.75 \times 10^{-4}]$. We will denote by $\tilde{c}_v = -1/\tilde{a}, \tilde{T}_v = -\tilde{b}/\tilde{a}$ the approximate blowup rate and blowup time obtained from this fitting procedure.

Since the quantities for which we would like to obtain the potential blowup rates are mostly the L^∞ norms of some solution functions, their values are sensitive to the discretization methods, the choice of the adaptive mesh, and the interpolation operations, especially when the maximum points are traveling as in our scenario. Therefore, the model (6.2) may not yield an ideal fitting even if the inverse power law (6.1) does exist, and the resulting $\tilde{c}_v$ may not reflect the true blowup rate c_v, though it should still be a good approximation. To obtain a better approximation of c_v, we will perform a local search near the crude estimate $\tilde{c}_v$ and find a value $\bar{c}_v$ such that the model

$$\gamma(t; v) := v(t)^{-1/\bar{c}_v} \sim \alpha^{-1/\bar{c}_v} (T-t)^{c_v/\bar{c}_v} \sim \alpha^{-1/c_v} (T-t) =: \bar{a}t + \bar{b} \tag{6.3}$$

has the best linear regression fitness (the R^2) against a least-squares test. More precisely, we put a uniform mesh (with 100 points) over the interval $[\tilde{c}_v - 0.1, \tilde{c}_v + 0.1]$, compute the R^2 value of the model (6.3) for each candidate blowup rate on the mesh, and find the blowup rate $\bar{c}_v$ such that the model (6.3) has the optimal fitness over all candidates. If $\bar{c}_v$ falls into one of the endpoints of the interval, i.e., $\tilde{c}_v \pm 0.1$, we will perform a local search again around $\bar{c}_v$ and update the value of $\bar{c}_v$. After this procedure, the resulting $\bar{c}_v$ should be a better approximation of c_v. Corresponding, $\bar{T} := -\bar{b}/\bar{a}$ is an approximation of the true blowup time T. Note that for the fitting of the model (6.3), we use the original recorded values of $v(t)$ rather than the time-interpolated values. We remark that the fitting of model (6.3) is more reliable than the fitting of model (6.2) in reflecting a potential inverse power law, as it is directly applied to the quantity of interest without taking the time derivative of the logarithm of this quantity. It is much harder for the logarithm of a blowup quantity to fall into the asymptotic regime in comparison with the blowup quantity itself. In other words, the fitting based on (6.3) is a refinement of the fitting based on (6.2).

6.2. Fitting of the growth rate. We are now ready to apply the above fitting procedures to the numerical solutions obtained in our computation. Figure 6.1 shows the fitting results for the quantity $\|u_1(t)\|_{L^\infty}$ (in Case 1) on the time interval $[t_1, t_2] = [1.6 \times 10^{-4}, 1.75 \times 10^{-4}]$. We can see that both models, $y(t; \|u_1\|_{L^\infty})$ and $\gamma(t; \|u_1\|_{L^\infty})$, have excellent linear fitness with R^2 values very close to 1 (the R^2 value for the model $\gamma(t; \|u_1\|_{L^\infty})$ is greater than $1 - 10^{-6}$). Note that the blowup rates (or the blowup times) learned from the two models are close to each other, cross-verifying

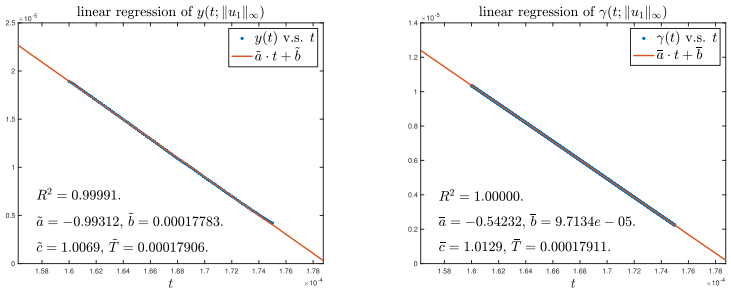

FIG 6.1. *The linear regression of* $y(t;\|u_1\|_{L^\infty})$ *(left) and* $\gamma(t;\|u_1(t)\|_{L^\infty})$ *(right) on the time interval* $[t_1,t_2]=[1.65\times10^{-4},1.75\times10^{-4}]$. *The blue points are the data points obtained from our computation, and the red lines are the linear models. We plot the linear models on a larger interval.*

the validity of both models. This strongly implies that $\|u_1\|_{L^\infty}$ has a finite-time singularity of an inverse power law with a blowup rate very close to 1, which is consistent with our observation and analysis in section 3.5. Recall that we have observed a strong positive alignment between $\psi_{1,z}$ and u_1 around the maximum point $R(t),Z(t)$ of u_1. In particular, $\psi_{1,z}(R(t),Z(t),t)\sim u_1(R(t),Z(t),t)$ in the stable phase $[1.6\times10^{-4},1.75\times10^{-4}]$. If we ignore the degenerate viscosity, then the equation of $\|u_1(t)\|_{L^\infty}$ can be approximated by

$$\frac{\mathrm{d}}{\mathrm{d}t}\|u_1(t)\|_{L^\infty}=2\psi_{1,z}(R(t),Z(t),t)\cdot u_1(R(t),Z(t),t)\sim c_0\|u_1(t)\|_{L^\infty}^2,$$

which then implies that $\|u_1(t)\|_{L^\infty}\sim(T-t)^{-1}$ for some finite time T. This asymptotic analysis is now supported by our linear fitting results.

Next, we study the growth of the maximum vorticity $\|\boldsymbol{\omega}\|_{L^\infty}$, which is an important indicator of a finite-time singularity. However, the growth of $\|\boldsymbol{\omega}\|_{L^\infty}$ may not reflect a clean inverse power law, since the maximum point of the vector magnitude $|\boldsymbol{\omega}|$ and the maximum points of the components $\omega^\theta,\omega^r,\omega^z$ are distinct in general. Therefore, we directly apply the fitting procedure to the maximums of the vorticity components instead of to the maximum vorticity. As an illustration, we present the study of the inverse power law of the axial vorticity component ω^z. Figure 6.2 shows the linear fitting for the associated models of $\|\omega^z(t)\|_{L^\infty}$ (in Case 1) on the time interval $[t_1,t_2]=[1.6\times10^{-4},1.75\times10^{-4}]$. Again, we see that both models $y(t;\|\omega^z\|_{L^\infty})$ and $\gamma(t;\|\omega^z\|_{L^\infty})$ have good linear fitness, which provides evidence of the finite-time blow of $\|\omega^z(t)\|_{L^\infty}$ in the form of an inverse power law

$$\|\omega^z(t)\|_{L^\infty}\sim(T-t)^{-\bar{c}_{\omega^z}}.$$

More importantly, the estimated blowup rate is approximately equal to 1.5, which implies that

$$\int_0^T\|\boldsymbol{\omega}(t)\|_{L^\infty}\geq\int_0^T\|\omega^z(t)\|_{L^\infty}\mathrm{d}t=+\infty.$$

According to our discussion in section 3.3, this strongly supports the existence of a finite-time singularity of the solution to the initial-boundary value problem (2.2)–(2.4) and (A.1).

To further illustrate the existence of a potential finite-time blowup, we perform the linear fitting procedure on more blowup quantities computed with different mesh

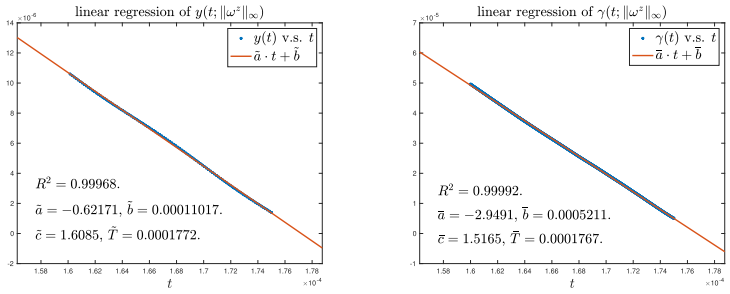

FIG 6.2. *The linear regression of $y(t;\|\omega^z\|_{L^\infty})$ (left) and $\gamma(t;\|\omega^z\|_{L^\infty})$ (right) on the time interval $[t_1,t_2] = [1.65\times10^{-4}, 1.75\times10^{-4}]$. The blue points are the data points obtained from our computation, and the red lines are the linear models. We plot the linear models on a larger interval.*

TABLE 6.1
Linear fitting results of model (6.3) *on time interval $[t_1,t_2] = [1.6\times10^{-4}, 1.75\times10^{-4}]$ for different solution quantities computed with different mesh sizes.*

Mesh size	$\|u_1\|_{L^\infty}$			$\|\omega_1\|_{L^\infty}$			$\|\psi_{1,r}\|_{L^\infty}$		
	$\bar{c}$	$\bar{T}/10^{-4}$	R^2	$\bar{c}$	$\bar{T}/10^{-4}$	R^2	$\bar{c}$	$\bar{T}/10^{-4}$	R^2
1024×512	1.0129	1.7911	1.00000	1.9773	1.7908	1.00000	1.1154	1.7998	0.99999
1536×768	1.0126	1.7914	1.00000	2.0366	1.7966	1.00000	1.1151	1.7975	0.99999
2048×1024	1.0125	1.7916	1.00000	2.0217	1.7956	1.00000	1.1129	1.7966	1.00000
Mesh size	$\|\psi_{1,z}\|_{L^\infty}$			$\|u_{1,r}\|_{L^\infty}$			$\|u_{1,z}\|_{L^\infty}$		
	$\bar{c}$	$\bar{T}/10^{-4}$	R^2	$\bar{c}$	$\bar{T}/10^{-4}$	R^2	$\bar{c}$	$\bar{T}/10^{-4}$	R^2
1024×512	0.9744	1.7952	0.99990	2.0427	1.7712	0.99993	1.9752	1.7687	0.99998
1536×768	0.9730	1.7954	0.99990	2.0445	1.7718	0.99993	1.9690	1.7690	0.99998
2048×1024	0.9724	1.7954	0.99991	2.0438	1.7719	0.99993	1.9666	1.7692	0.99998
Mesh size	$\|\omega^\theta\|_{L^\infty}$			$\|\omega^r\|_{L^\infty}$			$\|\omega^z\|_{L^\infty}$		
	$\bar{c}$	$\bar{T}/10^{-4}$	R^2	$\bar{c}$	$\bar{T}/10^{-4}$	R^2	$\bar{c}$	$\bar{T}/10^{-4}$	R^2
1024×512	1.5045	1.7950	1.00000	1.4878	1.7652	0.99997	1.5165	1.7670	0.99992
1536×768	1.5407	1.7937	1.00000	1.4912	1.7658	0.99997	1.5108	1.7648	0.99992
2048×1024	1.5270	1.7911	1.00000	1.4924	1.7661	0.99997	1.5097	1.7623	0.99993

resolutions. We only present the fitting results of model (6.3). Table 6.1 reports the linear fitting results of different solution quantities computed in Case 1 with different mesh sizes. Again, the fitting time interval is $[t_1,t_2] = [1.6\times10^{-4}, 1.75\times10^{-4}]$. We can see that all the quantities reported in the table have excellent fitting to some inverse power law, and the fitting results are consistent over different resolutions.

However, the estimated blowup times obtained from the fitting of different blowup quantities agree only up to the third digit. This may be due to the fact that the estimated blowup time is extrapolated information from the fitting model, which can be very sensitive to the recorded observations and the model parameters. In fact, if we force the blowup rate of $\|u_1\|_{L^\infty}$ to be $\bar{c} = 0.9$ (instead of $\bar{c} = 1.0129$) in model (6.3), then it still yields a fairly good linear regression with fitness $R^2 = 0.99945$, but the estimated blowup time drops to $\bar{T} = 1.7802$ (compared to 1.7911). Therefore, the estimated blowup time may not be a robust approximation of the true blowup time even if the finite-time singularity does exist. It is the estimated blowup rate that is more interesting in our analysis.

For the blowup rates reported in Table 6.1, we have the following observations and discussions. First, the fittings of $\|u_1\|_{L^\infty}, \|\psi_{1,z}\|_{L^\infty}$ again confirm the strong

alignment between u_1 and $\psi_{1,z}$. As we can see, the blowup rates of $\psi_{1,z}$ and u_1 are both close to 1, which is consistent with our observation that $\psi_{1,z} \sim u_1$ in the critical region around $(R(t), Z(t))$. This result supports our discussions on the blowup mechanism in section 3.5.

Moreover, there seems to be a pattern in the blowup rates of the quantities reported in Table 6.1. More precisely, we have the following approximation that agrees with the fitting results up to the first two digits:

$$\bar{c}_{u_1} \approx \bar{c}_{\psi_{1,r}} \approx \bar{c}_{\psi_{1,z}} \approx 1, \quad \bar{c}_{\omega^\theta} \approx \bar{c}_{\omega^r} \approx \bar{c}_{\omega^z} \approx 1.5, \quad \bar{c}_{\omega_1} \approx \bar{c}_{u_{1,r}} \approx \bar{c}_{u_{1,z}} \approx 2, \tag{6.4}$$

where we use $\bar{c}_f$ to denote the estimated blowup rate of $\|f(t)\|_{L^\infty}$ for a function $f(r,z,t)$. In the next section, we will argue that this pattern implies the existence of power laws for the two spatial scales of the solution, which is consistent with the direct linear fitting of these scales. Furthermore, this pattern reflects the possibility that the solution blows up in a locally self-similar way.

6.3. Fitting of spatial scalings. Recall that we have observed a two-scale property of the solution in our scenario: the smaller scale (featured by $Z(t)$) measures the length scale of the local solution profile near the point $(R(t), Z(t))$ (or the sharp front), and the larger scale (featured by $R(t)$) measures the distance between the sharp front and the symmetry axis $r = 0$. Our numerical observations suggest that these two scales are separated and both converge to 0, which characterizes the focusing nature of the blowup. The next step is to quantitatively investigate how fast these two scales go down to 0. Just like how we characterize the growth of the solution, we assume that these two spatial scales of the solution also admit some power laws:

$$C_s(t) = (T-t)^{c_s}, \quad C_l(t) = (T-t)^{c_l}, \tag{6.5}$$

where C_s denotes the larger scale (with a smaller power $c_s > 0$) and C_l the smaller scale (with a larger power $c_l > 0$). We will use two methods to check the validity of the power laws (6.5) and to learn the powers c_s, c_l, and we will compare the results from both methods to see if they are consistent.

The first method to learn the scalings of C_s, C_l is to extract the spatial information of the solution from the growth of different quantities. In fact, if the blowup solution develops a local profile of a isotropic spatial scale $C_l(t)$, it should be reflected by the spatial derivatives. More precisely, for a blowup function $f(r,z,t)$ that is smooth with respect to the scale $C_l(t)$, we should have

$$C_l(t) \sim \frac{\|f(t)\|_{L^\infty}}{\|f_r(t)\|_{L^\infty}} \sim \frac{\|f(t)\|_{L^\infty}}{\|f_z(t)\|_{L^\infty}},$$

which is equivalent to the relation

$$c_l = c_{f_r} - c_f = c_{f_z} - c_f,$$

if $f(t)$ also admits an inverse power law (6.1). We have seen in section 3.2 that the profile of u_1 is smooth when observed in a local neighborhood around $(R(t), Z(t))$, so we may use u_1 to extract the scaling of C_l. Our data in the previous subsection, particularly the pattern in (6.4), show that

$$\bar{c}_{u_{1,r}} - \bar{c}_{u_1} \approx \bar{c}_{u_{1,z}} - \bar{c}_{u_1} \approx 1,$$

which suggests that the solution has a local spatial scale

$$C_l(t) \sim Z(t) \sim T - t. \tag{6.6}$$

Similarly, we can learn the power of the larger scale C_s from our fitting of the growth of different blowup quantities. By the definition of u_1, ω_1, and $\boldsymbol{\omega}$, we have

$$\omega^\theta = r\omega_1, \quad \omega^r = -ru_{1,z}, \quad \omega^z = 2u_1 + ru_{1,r}. \tag{6.7}$$

We observe that the maximums of ω_1, $u_{1,z}$, $u_{1,r}$, ω^θ, ω^r, and ω^z are all achieved inside a local region around $(R(t), Z(t))$, whose length scale is featured by $Z(t) \ll R(t)$. It thus follows from (6.7) that

$$R(t) \sim \frac{\|\omega^\theta\|_{L^\infty}}{\|\omega_1\|_{L^\infty}} \sim \frac{\|\omega^r\|_{L^\infty}}{\|u_{1,z}\|_{L^\infty}} \sim \frac{\|\omega^z\|_{L^\infty}}{\|u_{1,r}\|_{L^\infty}},$$

which, ideally, is equivalent to the relations

$$c_s = c_{\omega^\theta} - c_{\omega_1} = c_{\omega^r} - c_{u_{1,z}} = c_{\omega^z} - c_{u_{1,r}}.$$

The data in Table 6.1 or the approximations in (6.4) yield that

$$\bar{c}_{\omega^\theta} - \bar{c}_{\omega_1} \approx \bar{c}_{\omega^r} - \bar{c}_{u_{1,z}} \approx \bar{c}_{\omega^z} - \bar{c}_{u_{1,r}} \approx 0.5,$$

which then suggests that

$$C_s(t) \sim R(t) \sim (T - t)^{0.5}. \tag{6.8}$$

The second method to verify the power laws (6.5) and to learn the powers c_s, c_l is by applying the fitting procedure in section 6.1 directly to the blowup quantities $R(t)^{-1}, Z(t)^{-1}$. Figure 6.3 presents the linear regression of model (6.3) for $R(t)^{-1}, Z(t)^{-1}$. We can see in Figure 6.3(left) that $R(t)$ has an excellent fitting to a power law with a rate $\bar{c}_s \approx 0.5$, which is very close to the conjectured power law (6.8) obtained from the first method.

Figure 6.3(right) shows that $Z(t)$ also approximately satisfies the power law with a rate $\bar{c}_l \approx 1$, though the fitness is not as good as that of $R(t)$. This lower fitness may be due to the issue that the numerical recording of $Z(t)$ is sensitive to the construction of the adaptive mesh and the interpolation operation between different meshes. Since $Z(t) \ll R(t)$, the relative error in $Z(t)$ due to discretization and interpolation

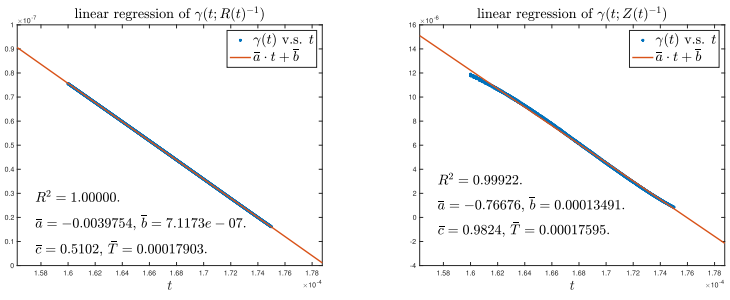

FIG 6.3. *The linear regression of $\gamma(t; R(t)^{-1})$ (left) and $\gamma(t; Z(t)^{-1})$ (right) on the time interval $[t_1, t_2] = [1.65 \times 10^{-4}, 1.75 \times 10^{-4}]$. The blue points are the data points obtained from our computation, and the red lines are the linear models. We plot the linear models on a larger interval.*

is expected to be much larger than the relative error in $R(t)$. Nevertheless, the estimated power of $Z(t)$, which is close to 1, is consistent with the conjectured power law (6.6).

The consistency between the numerical fitting results in this subsection and in the last subsection further confirms the validity of the (inverse) power laws (6.1), (6.5) of the solution, which provides additional supporting evidence for the existence of a finite-time singularity.

6.4. Locally self-similar structure. It is well known that the 3D Euler equations have the scaling invariance property that if $\boldsymbol{u}(x,t)$ is a solution to the equations, then

$$\boldsymbol{u}_{\lambda,\tau}(x,t) := \frac{\lambda}{\tau}\boldsymbol{u}\left(\frac{x}{\lambda}, \frac{t}{\tau}\right) \quad \text{for all } \lambda, \tau \in \mathbb{R}$$

is still a solution. Similarly, the 3D Navier–Stokes equations satisfy a more restricted scaling invariance property that if $\boldsymbol{u}(x,t)$ is a solution to the equations, then

$$\boldsymbol{u}_{\lambda}(x,t) := \frac{1}{\lambda}\boldsymbol{u}\left(\frac{x}{\lambda}, \frac{t}{\lambda^2}\right) \quad \text{for all } \lambda \in \mathbb{R}$$

is still a solution. Regarding these scaling properties, a fundamental question is whether the Euler equations or the Navier–Stokes equations have self-similar solutions of the form

$$\boldsymbol{u}(x,t) = \frac{1}{(T-t)^{\gamma}}\boldsymbol{U}\left(\frac{x-x_0}{(T-t)^{\beta}}\right), \tag{6.9}$$

where $\boldsymbol{U}$ is a self-similar vector profile and $\beta, \gamma > 0$ are scaling powers. If such a solution exists, it will imply that the Euler equations or the Navier–Stokes equations can develop a focusing self-similar singularity at the point x_0 at a finite time T.

The scaling properties of the Euler equations or the Navier–Stokes equations cannot hold in our scenario due to the existence of the cylinder boundary at $r = 1$ and the variable viscosity coefficients. Nevertheless, a focusing self-similar blowup can still exist asymptotically and locally near the symmetry axis $r = 0$ for two reasons. First of all, since the potential singularity is a focusing one around the origin $(r, z) = 0$, the solid boundary at $r = 1$ has no essential contribution to the blowup and can be neglected as a far field. Second, the variable viscosity coefficients in our scenario are degenerate near the origin and have an asymptotic behavior in the critical region that may be compatible with a self-similar blowup. More importantly, as we have seen in the previous subsections, the (inverse) power law fitting for the growth and the spatial scales of the solution and the consistency among the fitting results strongly suggest that the solution develops a finite-time self-similar singularity of the form (6.9).

However, the conventional self-similar ansatz (6.9) with a single spatial scaling is not suitable to characterize the potential two-scale blowup in our computation, since we have observed two separate spatial scales in the solution. To describe the locally self-similar two-scale blowup scenario, we propose the following self-similar ansatz with two spatial scales in the axisymmetric setting:

$$u_1(r,z,t) \sim (T-t)^{-c_u}\bar{U}\left(\frac{r-R(t)}{(T-t)^{c_l}}, \frac{z}{(T-t)^{c_l}}\right), \tag{6.10a}$$

$$\omega_1(r,z,t) \sim (T-t)^{-c_\omega}\bar{\Omega}\left(\frac{r-R(t)}{(T-t)^{c_l}}, \frac{z}{(T-t)^{c_l}}\right), \tag{6.10b}$$

$$\psi_1(r,z,t) \sim (T-t)^{-c_\psi} \bar{\Psi}\left(\frac{r-R(t)}{(T-t)^{c_l}}, \frac{z}{(T-t)^{c_l}}\right), \tag{6.10c}$$

$$R(t) \sim (T-t)^{c_s} R_0. \tag{6.10d}$$

Here $\bar{U}, \bar{\Omega}, \bar{\Psi}$ denote the self-similar profiles of u_1, ω_1, ψ_1, respectively. For notational simplicity, we use c_u, c_ω, c_ψ for $c_{u_1}, c_{\omega_1}, c_{\psi_1}$. As in our previous setting, the reference point $R(t)$ is chosen to be an r-coordinate of the maximum point of u_1, and $R_0 > 0$ is some normalization constant. This ansatz depicts that the solution develops an asymptotically self-similar blowup focusing at the point $(R(t), 0)$ with a local spatial length scale $(T-t)^{c_l}$, and in the meantime, the point $(R(t), 0)$ travels toward the origin with a different length scale $(T-t)^{c_s}$.

In what follows, we will carry out a numerical study of the solution profile in a local region around the dynamic location $(R(t), Z(t))$ (the maximum point of u_1) to further demonstrate the existence of a locally self-similar blowup of the form (6.10). After that, we will analyze the existence conditions and the properties of the self-similar profiles U, Ω, Ψ using a dynamic rescaling formulation of the equations (2.2).

6.5. Numerical evidence of locally self-similar profiles. An straightforward but useful way to identify a self-similar solution is by comparing the properly normalized profiles of the solution at different time instants. As we have mentioned, the self-similar ansatz (6.10) is not supposed to hold globally in the entire computational domain $\mathcal{D}_1$; it should only characterize the asymptotic blowup behavior of the solution in a local critical region. Therefore, it is important that we focus our study on the solution profile in a small-scale neighborhood of a reference point. In particular, the reference point is chosen to be $(R(t), Z(t))$, the maximum point of u_1.

Figure 6.4 compares the level sets of u_1 at different time instants. The first row of Figure 6.4 plots the level sets of u_1 in a local domain $(r,z) \in [0.8 \times 10^{-4}, 2.5 \times 10^{-4}] \times [0, 8 \times 10^{-6}]$. We can see that in a short time interval, from $t = 1.72 \times 10^{-4}$ to $t = 1.75 \times 10^{-4}$, the profile of u_1 changes remarkably. The main part of the profile shrinks in space and travels toward $z = 0$ in the z direction and toward the symmetry axis $r = 0$ in the r direction. The sharp front also becomes thinner and thinner. However, if we plot the level sets of the spatially rescaled function

$$\tilde{u}_1(\xi, \zeta, t) = u_1(Z(t)\xi + R(t), Z(t)\zeta, t) \tag{6.11}$$

as in the second row of Figure 6.4, we can see that the landscape of $\tilde{u}_1$ (in the $\xi\zeta$-plane) is almost static in the presented time interval. Here

$$\xi = \frac{r-R(t)}{Z(T)} \sim \frac{r-R(t)}{(T-t)^{c_l}}, \quad \zeta = \frac{z}{Z(T)} \sim \frac{z}{(T-t)^{c_l}}$$

are the shifted and rescaled coordinates motivated by the self-similar ansatz (6.10). This observation suggests that the asymptotic behavior (6.10a) of u_1 is valid and a self-similar profile $U(\xi, \zeta)$ exists.

Figure 6.5 compares the level sets of ω_1 and the level sets of the spatially rescaled function

$$\tilde{\omega}_1(\xi, \zeta, t) = \omega_1(Z(t)\xi + R(t), Z(t)\zeta, t) \tag{6.12}$$

in a similar manner. Again, we can see that this profile of ω_1 changes a lot in the presented time interval $t \in [1.72 \times 10^{-4}, 1.75 \times 10^{-4}]$, while the landscape of $\tilde{\omega}_1$ seems

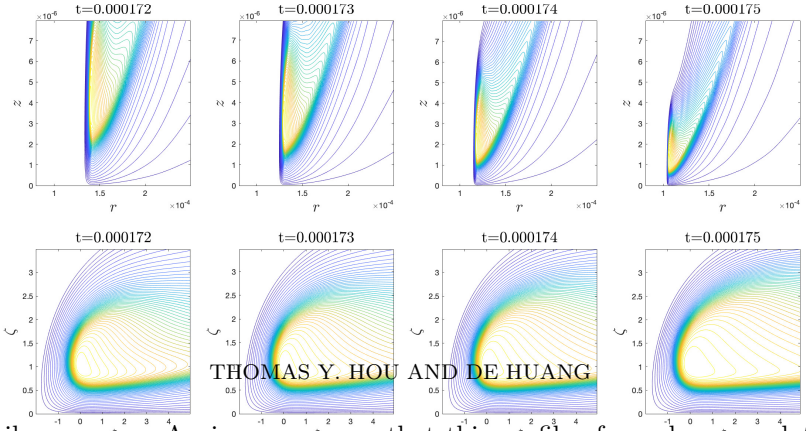

FIG 6.5. *Comparison of the level sets of ω_1 at different time instants. First row: original level sets of ω_1 in the domain $(r,z) \in [0.8\times10^{-4}, 2.5\times10^{-4}]\times[0, 8\times10^{-6}]$. Second row: rescaled level sets of ω_1 as a function of (ξ,ζ) in the domain $(\xi,\zeta) \in [-2,5]\times[0,3.5]$.*

Fig. 6.5. Comparison of the level sets of ω_1 at different time instants. First row: original level sets of ω_1 in the domain $(r,z) \in [0.8\times10^{-4}, 2.5\times10^{-4}]\times[0, 8\times10^{-6}]$. Second row: rescaled level sets of ω_1 as a function of (ξ,ζ) in the domain $(\xi,\zeta) \in [-2,5]\times[0,3.5]$.

34 THOMAS Y. HOU AND DE HUANG

in a similar manner. Again, we can see that this profile of ω_1 changes a lot in the presented time interval $t \in [1.72\times10^{-4}, 1.75\times10^{-4}]$, while the landscape of $\tilde{\omega}_1$ seems to converge. This further suggests the validity of the self-similar conjecture (6.10) for the solution.

Fig 6.5. Comparison of the level sets of ω_1 at different time instants. First row: original level sets of ω_1 in the domain $(r,z) \in [0.8\times10^{-4}, 2.5\times10^{-4}]\times[0, 8\times10^{-6}]$. Second row: rescaled level sets of ω_1 as a function of (ξ,ζ) in the domain $(\xi,\zeta) \in [-2,5]\times[0,3.5]$.

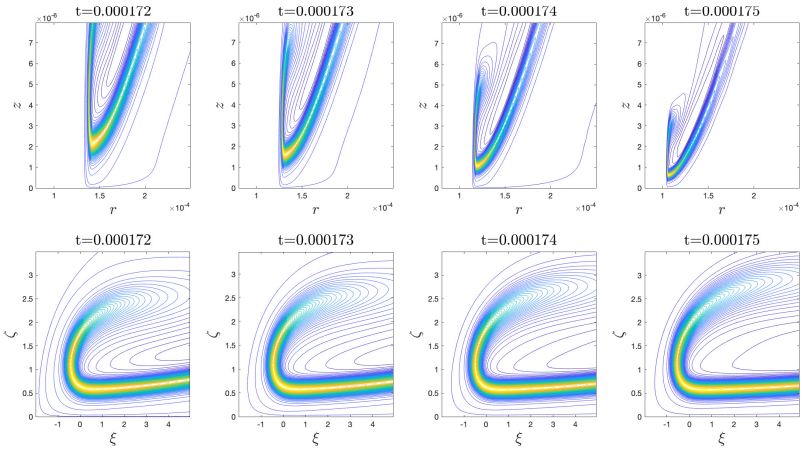

Second row: rescaled level sets of ω_1 as a function of $(\xi,\zeta) \in [-2,5]\times[0,3.5]$.

to converge. This further suggests the validity of the self-similar conjecture (6.10) for the solution.

We can also compare the cross sections of the solution at different time instants to study the potential self-similar blowup. As an example, Figure 6.6(a) and (c) present the evolution of the cross sections of u_1 through the point $R(t), Z(t)$ in both directions. The length scale of the profile shrinks in both directions, and the sharp front travels toward $r = 0$. For comparison, Figure 6.6(b) and (d) plot the corresponding cross sections of the normalized function $u_1/\|u_1\|_{L^\infty}$ in the rescaled coordinates $(r/R(t), z/Z(t))$, illustrating the potential convergence of the properly rescaled profile of u_1. Note that the rescaled cross sections in the r direction seem to converge only in a small neighborhood of $R(t)$, i.e., within $|r - R(t)| \equiv O(Z(t))$, implying that the asymptotic self-similar behavior (6.10a) is only valid locally. These results again support the existence of a locally self-similar profile of the solution near the reference point $(R(t), Z(t))$.

We can also compare the cross sections of the solution at different time instants to study the potential self-similar blowup. As an example, Figure 6.6(a) and (c) present the evolution of the cross sections of u_1 through the point $R(t), Z(t)$ in both directions. The length scale of the profile shrinks in both directions, and the sharp front travels toward $r = 0$. For comparison, Figure 6.6(b) and (d) plot the corresponding cross sections of the normalized function $u_1/\|u_1\|_{L^\infty}$ in the rescaled coordinates $(r/R(t), z/Z(t))$, illustrating the potential convergence of the properly rescaled profile of u_1. Note that the rescaled cross sections in the r direction seem to converge only in a small neighborhood of $R(t)$, i.e., within $|r - R(t)| \equiv O(Z(t))$, implying that the asymptotic self-similar behavior (6.10a) is only valid locally. These results again support the existence of a locally self-similar profile of the solution near the reference point $(R(t), Z(t))$.

6.6. Asymptotic analysis of self-similar blowup. In this subsection, we carry out an asymptotic analysis based on the self-similar ansztz (6.10) to provide a possible understanding of the two-scales features, blowup rates, and self-similar behaviors that we observed numerically.

A standard method to study a self-similar blowup is by substituting the self-

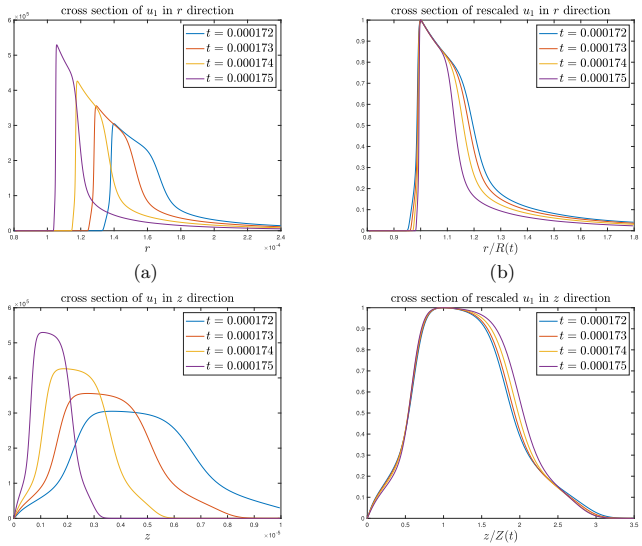

FIG 6.6. *Cross sections and rescaled cross sections of u_1 through the point $R(t), Z(t)$ in both directions at different time instants instants.* (a) *Cross sections in the r direction.* (b) *Rescaled cross sections in the r directions.* (c) *Cross sections in the z direction.* (d) *Rescaled cross sections in the z directions.*

support the existence of a locally self-similar profile of the solution near the reference point $(R(t), Z(t))$.

6.6. Asymptotic analysis of self-similar blowup. In this subsection, we carry out an asymptotic analysis based on the self-similar ansatz (6.10) to provide a possible understanding of the two-scales features, blowup rates and self-similar behaviors that we observed numerically.

A standard method to study a self-similar blowup is by substituting the self-similar ansatz (6.10) into the physical equations (2.2) and deriving equations for the potential self-similar profiles $\bar{U}, \bar{\Omega}, \bar{\Psi}$, based on the fundamental assumption that these profiles exist and are smooth functions. More appropriately, we will introduce time-dependent profile solutions U, Ω, Ψ and treat the potential self-similar profiles $\bar{U}, \bar{\Omega}, \bar{\Psi}$ as the steady state of U, Ω, Ψ. Thus, we can relate (u_1, ω_1, ψ_1) to (U, Ω, Ψ) by a dynamic change of variables given below:

$$u_1(r,z,t) = (T-t)^{-c_u} U(\xi, \zeta, \tau(t)), \tag{6.13a}$$

$$\omega_1(r,z,t) = (T-t)^{-c_\omega} \Omega(\xi, \zeta, \tau(t)), \tag{6.13b}$$

$$\psi_1(r,z,t) = (T-t)^{-c_\psi} \Psi(\xi, \zeta, \tau(t)), \tag{6.13c}$$

where

$$\xi := \frac{r - R(t)}{C_l(t)}, \quad \zeta := \frac{z}{C_l(t)}, \tag{6.13d}$$

and $\tau(t)$ is a rescaled time satisfying

$$\tau'(t) = (T-t)^{-1}. \tag{6.13e}$$

Now the self-similar ansatz (6.10) asserts that the profile solutions $U(\xi,\zeta,\tau), \Omega(\xi,\zeta,\tau)$, $\Psi(\xi,\zeta,\tau)$ in the $\xi\zeta$-coordinates should converge to some time-independent profiles $\bar{U}(\xi,\zeta), \bar{\Omega}(\xi,\zeta), \bar{\Psi}(\xi,\zeta)$ as $\tau \to \infty$ (i.e., $t \to T$). In particular, $\bar{U}, \bar{\Omega}, \bar{\Psi}$ should be smooth functions of ξ, ζ.

Before we derive the equations for the profile solutions U, Ω, Ψ, we first make some preparations to simplify our argument, so that we can focus on delivering the main idea. For simplicity, we only keep the viscosity terms (2.3) to their leading-order terms:

$$f_{u_1} \approx \nu^r \left(u_{1,rr} + \frac{3}{r} u_{1,r} \right) + \nu^z u_{1,zz}, \quad f_{\omega_1} \approx \nu^r \left(\omega_{1,rr} + \frac{3}{r} \omega_{1,r} \right) + \nu^z \omega_{1,zz}.$$

We remark that this approximation will not change the resulting equations for the self-similar profiles in the asymptotic analysis, since the terms that we have dropped are asymptotically small under our ansatz. Moreover, we assume that the ansatz (6.10d) is actually an identity:

$$R(t) = (T-s)^{c_s} R_0.$$

Guided by our numerical observations, we make the two-scale assumption:

$$c_s < c_l, \quad \text{or equivalently,} \quad R(t)/C_l(t) \to +\infty \quad \text{as} \quad t \to T. \tag{6.14}$$

Recall that $C_l := (T-t)^{c_l}$ (see the definition (6.5)). We will also use the following notation:

$$C_1(t) := (T-t)^{-1}, \quad C_u(t) := (T-t)^{-c_u}, \quad C_\omega(t) := (T-t)^{-c_\omega}, \quad C_\psi(t) := (T-t)^{-c_\psi}.$$

6.6.1. Substituting the self-similar ansatz. Now we substitute the change of variables (6.13) into the equations (2.2) (with the simplified viscosity terms). For clarity, we do this term by term. For the u_1 equation (2.2a), we have

$$\begin{aligned}
u_{1,t} &= C_1 C_u U_\tau + c_u C_1 C_u U + c_l C_1 C_u (\xi U_\xi + \zeta U_\zeta) + \underline{c_s C_1 C_u C_l^{-1} R U_\xi}, \\
u^r u_{1,r} + u^z u_{1,z} &= C_\psi C_u C_l^{-1} \big(-\xi \Psi_\zeta U_\xi + (2\Psi + \xi \Psi_\xi) U_\zeta \big) \\
&\quad + \underline{C_\psi C_u C_l^{-2} R \big(-\Psi_\zeta U_\xi + \Psi_\xi U_\zeta \big)}, \\
2\psi_{1,z} u_1 &= 2 C_\psi C_u C_l^{-1} \Psi_\zeta U, \\
f_{u_1} &= C_u C_l^{-2} \big(\nu^r U_{\xi\xi} + 3\nu^r (\xi + R C_l^{-1})^{-1} U_\xi + \nu^z U_{\zeta\zeta} \big).
\end{aligned} \tag{6.15a}$$

Note that we have used the expressions of u^r, u^z in (2.2d). We have also used the relation (6.13e): $\tau'(t) = (T-t)^{-1} = C_1$. Similarly, for the ω_1 equation (2.2b), we have

$$\begin{aligned}
\omega_{1,t} &= C_1 C_\omega \Omega_\tau + c_\omega C_1 C_\omega \Omega + c_l C_1 C_\omega (\xi \Omega_\xi + \zeta \Omega_\zeta) + \underline{c_s C_1 C_\omega C_l^{-1} R \Omega_\xi}, \\
u^r \omega_{1,r} + u^z \omega_{1,z} &= C_\psi C_\omega C_l^{-1} \big(-\xi \Psi_\zeta \Omega_\xi + (2\Psi + \xi \Psi_\xi) \Omega_\zeta \big) \\
&\quad + \underline{C_\psi C_\omega C_l^{-2} R \big(-\Psi_\zeta \Omega_\xi + \Psi_\xi \Omega_\zeta \big)}, \\
2 u_{1,z} u_1 &= 2 C_u^2 C_l^{-1} U_\zeta U, \\
f_{\omega_1} &= C_\omega C_l^{-2} \big(\nu^r \Omega_{\xi\xi} + 3\nu^r (\xi + R C_l^{-1})^{-1} \Omega_\xi + \nu^z \Omega_{\zeta\zeta} \big).
\end{aligned} \tag{6.15b}$$

Finally, for the Poisson equation (2.2c), we have

(6.15c)
$$-\left(\partial_r^2+\frac{3}{r}\partial_r+\partial_z^2\right)\psi_1=\omega_1 \quad \Longrightarrow \quad -C_\psi C_l^{-2}\left(\partial_\xi^2+\frac{3}{\xi+RC_l^{-1}}\partial_\xi+\partial_\zeta^2\right)\Psi=C_\omega\Omega.$$

6.6.2. Balancing the equations. The next step is to determine the relations between the quantities C_u, C_ω, C_ψ, C_l, and R by balancing the terms in each equation of (6.15) in the asymptotic regime $t\to T$, based on the assumption that the limit profiles $\bar{U},\bar{\Omega},\bar{\Psi}$ are smooth functions of ξ,ζ and are independent of time t. We also assume that the viscosity term is of the same order as the vortex stretching term. This balance is crucial in determining the length scale for C_l or $Z(t)$.

We have underlined some terms in (6.15a) and (6.15b) for reasons to be clarified later. For those terms that are not underlined in (6.15a), the balance among various terms as $t\to T$ requires

$$C_1C_u=C_\psi C_uC_l^{-1}\sim\nu C_uC_l^{-2}.$$

Similarly, for those terms that are not underlined in (6.15b), the balance among various terms as $t\to T$ enforces

$$C_1C_\omega=C_\psi C_\omega C_l^{-1}=C_u^2C_l^{-1}\sim\nu C_\omega C_l^{-2}.$$

Finally, for the Poisson equation (6.15c) to balance as $t\to T$, we must have

$$C_\psi C_l^{-2}=C_\omega.$$

Summarizing these relations, we obtain

$$\text{(6.16)}\qquad \begin{cases} C_u=C_1,\\ C_\omega=C_1C_l^{-1},\\ C_\psi=C_1C_l, \end{cases} \quad\Longleftrightarrow\quad \begin{cases} c_u=1,\\ c_\omega=1+c_l,\\ c_\psi=1-c_l, \end{cases}$$

and

$$\text{(6.17)}\qquad \nu^r\sim\nu^z\sim C_1C_l^2=(T-t)^{2c_l-1}.$$

Note that the relations (6.16) also imply that the underlined terms can balance with each other in (6.15a) and in (6.15b).

So far, we have already obtained some meaningful information of the blowup rates. If the self-similar ansatz (6.10) is true, then no matter what the spatial scalings c_s,c_l are, the asymptotic blowup rates of $u_1,\psi_{1,r},\psi_{1,z}$ are always 1:

$$\|u_1\|_{L^\infty}\sim C_u=C_1=(T-t)^{-1},\quad \|\psi_{1,r}\|_{L^\infty}\sim\|\psi_{1,z}\|_{L^\infty}\sim C_\psi C_l^{-1}=C_1=(T-t)^{-1}.$$

This result of the asymptotic analysis is consistent with our observations and fitting results in section 6.2, which confirms the validity of the inverse power law for u_1. To obtain the blowup rate of ω_1, we still need to determine the value of c_l.

6.6.3. Conservation of circulation. To determine the values of c_s,c_l, we need to make use of the conservation of the total circulation, an important physical property of the axisymmetric Euler or Navier–Stokes equations.

The total circulation is defined as

$$\Gamma(r,z,t) := ru^\theta(r,z,t) = r^2 u_1(r,z,t).$$

It is easy to derive the equation of Γ from the u_1 equation (2.2a):

$$\Gamma_t + u^r\Gamma_r + u^z\Gamma_z = r^2 f_{u_1}. \tag{6.18}$$

Recall that f_{u_1} is the viscosity term in the u_1 equation (2.2a). In our scenario, Γ is a nonnegative variable in the computational domain $\mathcal{D}_1$, since $u_1 \geq 0$ in $\mathcal{D}_1$. It is well known that the circulation function Γ satisfies a maximum principle for the Euler equations or the Navier–Stokes equations. In fact, it also satisfies a maximum principle for our equations (2.2). Let $(\tilde{R}(t), \tilde{Z}(t))$ be a local maximum point of Γ; then we have from (6.18) that

$$\frac{\mathrm{d}}{\mathrm{d}t}\Gamma(\tilde{R},\tilde{Z},t) = \nu^r\Gamma_{rr} + \nu^z\Gamma_{zz} - \frac{\nu_r^r}{\tilde{R}}\Gamma \leq 0,$$

where we have used that $\Gamma_{rr}, \Gamma_{zz} \leq 0$ at the local maximum point $(\tilde{R}(t), \tilde{Z}(t))$, and that $\nu_r^r \geq 0$ for the variable viscosity coefficient we use in our computation. This means that $\Gamma(\tilde{R}(t), \tilde{Z}(t), t)$ is always nonincreasing in time.

In fact, we have observed that the maximum point $(R(t), Z(t))$ of u_1 is also a local maximum point of Γ. Therefore,

$$\frac{\mathrm{d}}{\mathrm{d}t}\Gamma(R(t),Z(t),t) = \nu^r\Gamma_{rr} + \nu^z\Gamma_{zz} - \frac{\nu_r^r}{R}\Gamma \leq 0.$$

The viscosity term $\nu^r\Gamma_{rr} + \nu^z\Gamma_{zz}$ cannot damp $\Gamma(R,Z,t)$ to 0 in a finite time as long as the viscosity coefficients are bounded, which is the case in our computation. From the expression (A.3a) of ν_r, we have $\nu_r^r = O(r)$ in the critical blowup region and thus $\nu_r^r(R,Z)/R = O(1)$. Therefore, the term $-\nu_r^r\Gamma/R$ is a linear damping term with an $O(1)$ coefficient, which can only drive Γ to 0 as $t \to +\infty$. In summary, $\Gamma(R,Z,t)$ will not blow up or vanish to 0 in any finite time T. That is, $\Gamma(R,Z,t) = R^2 u_1(R,Z,t) = O(1)$ as $t \to T$. It follows from the blowup scaling of u_1 that

$$R(t) \sim \|u_1\|_{L^\infty}^{-1/2} \sim (T-t)^{c_u/2} = (T-t)^{1/2},$$

which implies

$$c_s = 1/2.$$

We remark that this property only relies on the conservation of the maximum circulation and the fact that $c_u = 1$, which are intrinsic to the equations (2.2).

6.6.4. Determining the smaller scale. To determine c_l, we need to use again the asymptotic values of the variable viscosity coefficients,

$$\nu^r \sim \nu^z = O(r^2) + O(z^2) + 0.025\,\|\omega^\theta\|_{L^\infty}^{-1},$$

for r, z close to 0, which follows from the expressions (A.3). In particular, in the critical region around the reference point $(R(t), Z(t))$ where the self-similar ansatz (6.10) is assumed to be valid, we have

$$\begin{aligned}\nu^r \sim \nu^z &= O(R^2) + O(Z^2) + O(R^{-1}\|\omega_1\|_{L^\infty}^{-1}) \\ &= O((T-t)^{2c_s}) + O((T-t)^{2c_l}) + O((T-t)^{1+c_l-c_s}) \sim (T-t)^1,\end{aligned}$$

where we have used $c_s = 1/2$ and the two-scale assumption (6.14) that $c_l > c_s$, so that $O((T-t)^{2c_l})$ and $O((T-t)^{1+c_l-c_s})$ are dominated by $O((T-t)^{2c_s})$. Comparing this with the relation (6.17), we conclude that $2c_l - 1 = 1$, that is, $c_l = 1$.

We have now obtained all the blowup rates and the spatial scalings in the self-similar ansatz (6.10):

$$c_s = 1/2, \quad c_l = 1, \quad c_u = 1, \quad c_\omega = 1 + c_l = 2, \quad c_\psi = 1 - c_l = 0. \tag{6.19a}$$

Moreover, the derivative relations and product relations yield that

$$\begin{aligned} &c_{\psi_{1,r}} = c_{\psi_{1,z}} = c_\psi + c_l = 1, \quad c_{u_{1,r}} = c_{u_{1,z}} = c_u + c_l = 2, \\ &c_{\omega^\theta} = c_\omega - c_s = 1.5, \quad c_{\omega^r} = c_{u_{1,z}} - c_s = 1.5, \quad c_{\omega^z} = c_{u_{1,r}} - c_s = 1.5. \end{aligned} \tag{6.19b}$$

These results are surprisingly consistent with the fitting data in sections 6.2 and 6.3, especially the numerically observed pattern (6.4). The consistency between the blowup rates obtained by our numerical fitting procedures and those obtained by the asymptotic scaling analysis provides further support for the existence of a finite-time locally self-similar blowup of the form (6.10).

We remark that if we use a constant viscosity coefficient $\nu^r = \nu^z = \mu$, then through a similar balancing procedure we will obtain a different scaling result with $c_l = 1/2$. This implies that there is no two-scale feature in the potential blowup solution, which is consistent with our numerical observations. This also explains why the two-scale blowup cannot survive the viscosity with a constant coefficient in Case 2 computation, as we have seen in section 4.

6.6.5. Equations for the self-similar profiles. Our previous analysis on the blowup rates is based on the fundamental assumption that the asymptotic self-similar profiles $\bar{U}, \bar{\Omega}, \bar{\Psi}$ exist, for which we present strong numerical evidence in the previous sections. To gain more insights into the locally self-similar blowup, we will derive some potential time-independent equations for the self-similar profiles, which may help us understand the properties and the existence conditions of these profiles.

Collecting the terms in (6.15a), (6.15b), and (6.15c) and using the relations in (6.16) and (6.17), we first obtain the following time-dependent equations for the dynamic profiles:

$$\begin{aligned} &U_\tau + (c_l\xi - \xi\Psi_\zeta)U_\xi + (c_l\zeta + 2\Psi + \xi\Psi_\xi)U_\zeta + \underline{RC_l^{-1}\big((c_s - \Psi_\zeta)U_\xi + \Psi_\xi U_\zeta\big)} \\ &\qquad = 2\Psi_\zeta U - c_u U + \tilde{\nu}^r\big(U_{\xi\xi} + 3(\xi + RC_l^{-1})U_\xi\big) + \tilde{\nu}^z U_{\zeta\zeta}, \end{aligned} \tag{6.20a}$$

$$\begin{aligned} &\Omega_\tau + (c_l\xi - \xi\Psi_\zeta)\Omega_\xi + (c_l\zeta + 2\Psi + \xi\Psi_\xi)\Omega_\zeta + \underline{RC_l^{-1}\big((c_s - \Psi_\zeta)\Omega_\xi + \Psi_\xi\Omega_\zeta\big)} \\ &\qquad = 2U_\zeta U - c_\omega\Omega + \tilde{\nu}^r\big(\Omega_{\xi\xi} + 3(\xi + RC_l^{-1})\Omega_\xi\big) + \tilde{\nu}^z\Omega_{\zeta\zeta}, \end{aligned} \tag{6.20b}$$

$$-\big(\partial_{\xi\xi} + 3(\xi + RC_l^{-1})^{-1}\partial_\xi + \partial_{\zeta\zeta}\big)\Psi = \Omega, \tag{6.20c}$$

where

$$\tilde{\nu}^r(\xi,\zeta) := (T-t)^{-1}\nu^r(C_l\xi + R(t), C_l\zeta), \quad \tilde{\nu}^z(\xi,\zeta) := (T-t)^{-1}\nu^z(C_l\xi + R(t), C_l\zeta).$$

For the self-similar profiles to exist, it requires that the solution to the equations (6.20) converges to some nontrivial steady state $\bar{U}, \bar{\Omega}, \bar{\Psi}$ as $\tau \to \infty$. We thus expect that each equation of (6.20) is balanced in the limit $\tau \to \infty$. Note that from the relation

(6.13e) we have $\tau = -\log(T-t)+c$ for some constant c, so $\tau\to\infty$ means $t\to T$. Since we have argued that $R(t)/C_l(t)\sim (T-t)^{-1/2}\to\infty$ as $t\to T$, the underlined terms in (6.20a) and (6.20b) need to satisfy some extra conditions so that they can balance with the other terms. In particular, we should have

$$RC_l^{-1}\big((c_s-\Psi_\zeta)U_\xi+\Psi_\xi U_\zeta\big)\to G_u(\xi,\zeta),\quad RC_l^{-1}\big((c_s-\Psi_\zeta)\Omega_\xi+\Psi_\xi\Omega_\zeta\big)\to G_\omega(\xi,\zeta)$$

for some smooth functions $G_u, G_\omega = O(1)$ as $t\to T$. This further implies that

$$(c_s-\Psi_\zeta)U_\xi+\Psi_\xi U_\zeta\to 0\quad\text{and}\quad (c_s-\Psi_\zeta)\Omega_\xi+\Psi_\xi\Omega_\zeta\to 0\quad\text{as } t\to T.$$

Moreover, since $R(t)/C_l(t)\to\infty$ as $t\to T$, the lower order viscosity term $3(\xi + RC_l^{-1})^{-1}\partial_\xi$ in (6.20a), (6.20b) and in the Poisson equation (6.20c) should vanish as $t\to T$.

Based on the preceding discussions, we conjecture the following time-independent equations for the self-similar profiles $\bar U,\bar\Omega,\bar\Psi$:

$$(c_l\xi-\xi\bar\Psi_\zeta)\bar U_\xi+(c_l\zeta+2\bar\Psi+\xi\bar\Psi_\xi)\bar U_\zeta+G_u=2\bar\Psi_\zeta\bar U-c_u\bar U+\bar\nu^r\bar U_{\xi\xi}+\bar\nu^z\bar U_{\zeta\zeta},\tag{6.21a}$$

$$(c_l\xi-\xi\bar\Psi_\zeta)\bar\Omega_\xi+(c_l\zeta+2\bar\Psi+\xi\bar\Psi_\xi)\bar\Omega_\zeta+G_\omega=2\bar U_\zeta\bar U-c_\omega\bar\Omega+\bar\nu^r\bar\Omega_{\xi\xi}+\bar\nu^z\bar\Omega_{\zeta\zeta},\tag{6.21b}$$

$$-(\partial_{\xi\xi}+\partial_{\zeta\zeta})\bar\Psi=\bar\Omega,\tag{6.21c}$$

$$(c_s-\bar\Psi_\zeta)\bar U_\xi+\bar\Psi_\xi\bar U_\zeta=0,\tag{6.21d}$$

$$(c_s-\bar\Psi_\zeta)\bar\Omega_\xi+\bar\Psi_\xi\bar\Omega_\zeta=0,\tag{6.21e}$$

where

$$\bar\nu^r(\xi,\zeta):=\lim_{t\to T}(T-t)^{-1}\nu^r(R(t),0),\quad \bar\nu^z(\xi,\zeta):=\lim_{t\to T}(T-t)^{-1}\nu^z(R(t),0).$$

The existence of the self-similar profiles of the above equations is beyond the scope of this paper. We remark that our preceding asymptotic scaling analysis is valid when we properly rescale the solution and zoom in to an $O(C_l(t))$ neighborhood of the point $(R(t),0)$ in the rz-plane. From a 3D macroscopic perspective, one may view the blowup region of the solution as a tubular ring surrounding the symmetry axis with a decreasing radius $R(t)$ and a shrinking thickness $C_l(t)$. Correspondingly, the equations (6.21) only characterize the asymptotic self-similar behavior of the solution on the scale of $C_l(t)$ in the limit $t\to T$ around the 1D ring $\{(r,z,\theta)|r=R(t),z=0,\theta\in[0,2\pi)\}$. If we zoom out to an $O(R(t))$ region around the origin, we can only see the blowup region shrinking into a 1D ring, and hence we cannot see the effect of these equations. Therefore, we say that the potential two-scale blowup in our scenario is only locally self-similar with respect to the smaller scale $C_l(t)$.

6.6.6. A level set condition. Though we cannot use the equations (6.21) to determine the self-similar profiles $\bar U,\bar\Omega,\bar\Psi$, we can still learn some properties of the profiles from them. Note that (6.21d) and (6.21e) are independent of the unknown functions G_u, G_ω, and it thus makes sense to study their implications. One can see these two equations as necessary conditions for the self-similar profiles to exist. The physical solutions u_1,ω_1,ψ_1 can only develop the two-scale self-similar blowup when

The physical solutions satisfy these two conditions locally (or after rescaling). If these two conditions are not satisfied locally, the underlined terms in equations (6.20) will not be compatible with our preceding scaling analysis based on the balance of scales among various terms.

Let $\Phi(\xi,\zeta) = \Psi(\xi,\zeta) - c_s\zeta$. Then (6.21d) and (6.21e) can be written as

$$\Phi_\xi U_\zeta - \Phi_\zeta U_\xi = 0, \quad \Phi_\xi \Omega_\zeta - \Phi_\zeta \Omega_\xi = 0, \tag{6.22}$$

which implies that the gradients of U, Ω, Φ are parallel to each other,

$$(U_\xi, U_\zeta) \parallel (\Omega_\xi, \Omega_\zeta) \parallel (\Phi_\xi, \Phi_\zeta),$$

or that the level sets of U, Ω, Φ have the same geometric contours. In other words, the profiles U, Ω, Φ can be viewed as functions of each other:

$$U = U(\Phi), \quad \Omega = \Omega(\Phi).$$

The above relationship also implies that the velocity field induced by the modified stream function Φ is parallel to the level set of U and Ω. In other words, the large underlined advection terms in (6.20a) and (6.20b) enforce a condition that the local velocity field near the sharp front should be tangent to the sharp front. This also provides us a way to numerically verify the condition (6.22). Note that under the asymptotic ansatz (6.10), we have

$$(u_{1,r}, u_{1,z}) \parallel (U_\xi, U_\zeta) \quad \text{and} \quad (\omega_{1,r}, \omega_{1,z}) \parallel (\Omega_\xi, \Omega_\zeta),$$

which means that if U is a function of Ω, then u_1 is also a function of ω_1:

$$(u_{1,r}, u_{1,z}) \parallel (\omega_{1,r}, \omega_{1,z}). \tag{6.23}$$

We can thus examine the validity of the condition (6.22) by comparing the level sets of u_1 and ω_1.

Figure 6.7 compares the level sets of the stretched and shifted functions

$$\begin{aligned} \tilde{u}_1(\xi,\zeta,t) &= u_1(C_l(t)\xi + R(t), C_l(t)\zeta, t), \\ \tilde{\omega}_1(\xi,\zeta,t) &= \omega_1(C_l(t)\xi + R(t), C_l(t)\zeta, t), \\ \text{and} \quad \tilde{\phi}_1(\xi,\zeta,t) &= \psi_1(C_l(t)\xi + R(t), C_l(t)\zeta, t) - c_s\zeta \end{aligned}$$

at $t = 1.76 \times 10^{-4}$ in the $\xi\zeta$-plane. These functions are the same as U, Ω, Φ up to rescaling in magnitude. As we can see, though the contours of these functions are

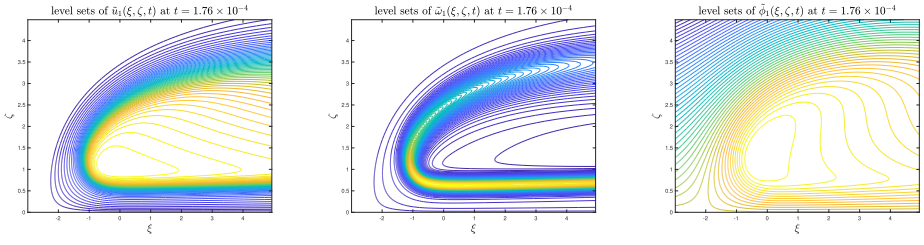

FIG 6.7. *Level sets of the stretched functions* $\tilde{u}_1$ *(left),* $\tilde{\omega}_1$ *(middle), and* $\tilde{\phi}_1$ *(right) at* $t = 1.76 \times 10^{-4}$.

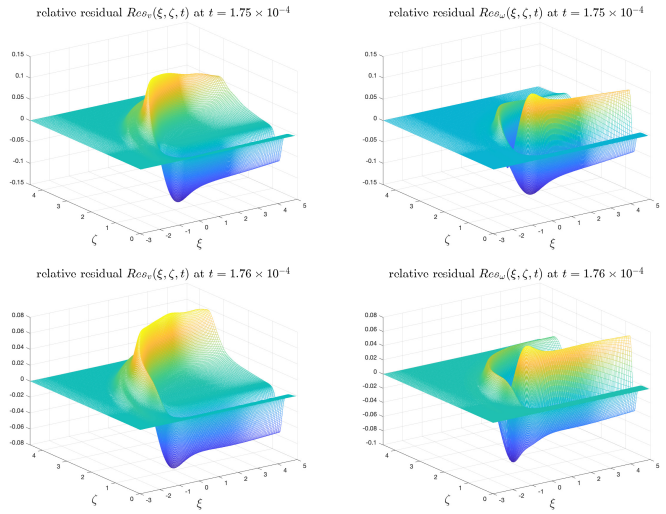

FIG 6.8. *The relative residuals* $Res_u(\xi,\zeta,t)$ *and* $Res_\omega(\xi,\zeta,t)$ *at* $t = 1.75 \times 10^{-4}$ *(upper row) and* $t = 1.76 \times 10^{-4}$ *(lower row).*

not exactly the same in the local neighborhood (of length scale $Z(t)$) of the point $(R(t), Z(t))$, they have surprising geometric similarities. In particular, the level sets of $\tilde{u}_1$ and $\tilde{\omega}_1$ are almost parallel to each other along the curved band where lies the thin structure of $\tilde{\omega}_1$. We also notice that the level sets of $\tilde{\phi}_1$ are less geometrically similar to those of $\tilde{u}_1$ and $\tilde{\omega}_1$, which is possibly because the rescaling constant $c_s = 1/2$ is only valid in the asymptotic limit $t \to T$.

To further justify the level set condition, we investigate the (time-dependent) relative residuals of the equations in (6.22). The relative residual Res_u of the first equation is defined as

$$Res_u(\xi,\zeta,t) = \frac{\tilde{\phi}_{1,\xi}\tilde{u}_{1,\zeta} - \tilde{\phi}_{1,\zeta}\tilde{u}_{1,\xi}}{M_u(t)}, \quad \text{where} \quad M_u(t) = \max_{\xi,\zeta} \sqrt{(\tilde{\phi}_{1,\xi}\tilde{u}_{1,\zeta})^2 + (\tilde{\phi}_{1,\zeta}\tilde{u}_{1,\xi})^2}.$$

The relative residual $Res_\omega(\xi,\zeta,t)$ of the second equation is defined similarly. Figure 6.8 shows the profiles of Res_u and Res_ω at two time instants $t_1 = 1.75 \times 10^{-4}$ and $t_2 = 1.76 \times 10^{-4}$ in the late stage of our computation. One can see that the magnitudes of the relative residuals are reasonably small and their maximums are decreasing in time, from $(\|Res_u(t_1)\|_{L^\infty}, \|Res_\omega(t_1)\|_{L^\infty}) = (0.1288, 0.1231)$ to $(\|Res_u(t_2)\|_{L^\infty}, \|Res_\omega(t_2)\|_{L^\infty}) = (0.0723, 0.0849)$.

These numerical observations are strong evidence of the validity of the condition (6.22) in the critical blowup region and partial justification of our asymptotic analysis of the potential locally self-similar blowup. As mentioned above, we can also understand this interesting phenomenon from a different angle: it is because the level set condition (6.23) is well satisfied in a local region around $(R(t), Z(t))$ that the solution can possibly develop a locally self-similar blowup in the form of (6.10).

6.7. On the choice of viscosity coefficients. As we have demonstrated in the previous subsection, the fact that $c_u = 1$ and $c_s = 1/2$, i.e.,

$$\|u_1(t)\|_{L^\infty} \sim (T-t)^{-1}, \quad R(t) \sim (T-t)^{1/2},$$

is an intrinsic property of the equations (2.2), which does not depend on the choice of the viscosity coefficients (though we have used that $\nu_r^r \geq 0$, but it is not essential). However, the conclusion $c_l = 1$ and its consequences (such as $c_\omega = 2$) rely on the particular asymptotic behavior of the degenerate viscosity coefficients,

$$\nu^r \sim \nu^z \sim R(t)^2 \sim (T-t)^1,$$

which does not seem to be essential to the potential blowup.

We have also solved the initial-boundary value problem (2.2)–(2.4) and (A.1) with stronger or weaker viscosity but failed to observe convincing evidence of a sustainable (self-similar) blowup. Since the smooth viscosity coefficients are even functions of r and z (see section 2.2), we can only choose ν^r, ν^z to have the asymptotic behavior

$$\nu^r, \nu^z = O(r^{2p}) + O(z^{2q})$$

for some integers p, q, where we have ignored the time-dependent part of ν^r, ν^z. If the viscosity is too strong $(p, q = 0)$, the two-scale feature cannot survive and there is no blowup observed, as we have reported in section 4. If the viscosity is too weak or if there is no viscosity, the solution quickly becomes very unstable in the early stage of the computation before a stable self-similar blowup can be observed. Even in the case of $p = q = 1$, the constants in front of r^2 and z^2 need to be chosen carefully so that the viscosity is strong enough to control the mild oscillations in the tail region.

It would be interesting to investigate whether the scale $c_l = 1$ is intrinsic to the two-scale singularity or it is determined by the order of degeneracy $O(r^2) + O(z^2)$ in our variable viscosity coefficients. We plan to investigate this question by applying degenerate viscosity coefficients with different orders of degeneracy at the origin. As in the case of $p = q = 1$, the constants in front of r^{2p} and z^{2q} need to be chosen so that the viscosity is strong enough to control the mild oscillations in the tail region. We shall leave this question to our future work.

7. Concluding remarks. In this paper, we presented strong numerical evidence that the axisymmetric Euler equations with degenerate variable viscosity coefficients develop a finite-time singularity at the origin. An important feature of this potential singularity is that the solution develops a two-scale traveling wave solution that travels toward the origin. The antisymmetric vortex dipole and the odd symmetry in the initial data generate a strong shear flow that pushes the solution toward the symmetry plane $z = 0$ rapidly. The flow is then transported toward the symmetry axis $r = 0$ by the strong negative radial velocity induced by the vortex dipole. The hyperbolic flow structure near the center of the traveling wave generates a no-spinning region near the symmetry axis within which the angular velocity is almost zero. The special design of our initial data and the dynamic formation of this no-spinning region generate a positive feedback loop that enforces strong nonlinear alignment in vortex stretching, leading to a potential locally self-similar blowup at the origin. We performed a resolution study and an asymptotic scaling analysis to provide further support of the potential locally self-similar blowup.

The degeneracy of the variable viscosity coefficients at the origin plays an essential role in stabilizing this potential singularity formation for the incompressible axisymmetric Euler equations. We have also studied the incompressible Navier–Stokes equations with constant viscosity coefficient using the same initial data. Our numerical study revealed that the constant viscosity regularizes the smaller scale of the two-scale traveling wave solution and destabilizes the nonlinear alignment in the vortex

stretching term. The solution of the Navier–Stokes equation with constant viscosity coefficient behaves completely differently. We did not observe the finite-time singularity formation that we observed for the Euler equations with degenerate variable viscosity coefficients.

We also performed some preliminary study of the 3D Euler equations using the same initial data. Our study showed that the solution of the Euler equations grows even faster than the solution of the 3D Euler equations with degenerate viscosity coefficients during the warm-up phase. However, the Euler solution quickly developed a very thin structure near the sharp front before the nonlinear vortex stretching had a chance to develop a strong alignment. Without viscous regularization, the thickness of the sharp front collapses to zero faster than $Z(t)$. Thus, the solution of the 3D Euler equations seems to develop a 3-scale structure, which is extremely difficult to resolve numerically. We presented some preliminary numerical evidence that seems to indicate that the 3D Euler equations may develop a potentially singular behavior in a way similar to that of the 3D Euler equations with degenerate viscosity coefficients. However, without viscous regularization, we were not able to produce convincing numerical evidence for the potential blowup of the 3D Euler equations. On the other hand, by applying a first-order numerical viscosity plus a time-dependent vanishing viscosity of order $O(R(t)^2) + O(Z(t)^2)$, we obtained strong numerical evidence that the 3D Euler equations develop a finite-time singularity with scaling properties similar to those of the Euler equations with degenerate viscosity coefficients; see [HH22a] for more discussion.

Our current computation still suffers from two limitations. The first one is that our adaptive mesh strategy would break down in the limit of $R(t)/Z(t) \to \infty$. We need to develop a more effective adaptive mesh strategy to overcome this difficulty. The second one is that as we approach the singularity time, the shearing induced oscillations in the tail region become more severe. We need to apply stronger filtering in the tail region to control these oscillations in the tail region, which compromises the accuracy of our computation unless we use a very fine mesh. We hope to address these limitations in our future work.

Appendix A. Initial data and variable viscosity coefficients. In this appendix, we describe how to construct our initial data and the variable viscosity coefficients.

A.1. Initial data. We construct the initial data based on our empirical insights and understanding of the potential blowup scenario that we shall explain later. The initial data are given by

(A.1)
$$u_1^0(r,z) = m_u^{(1)} \frac{u_1^{(1)}(r,z)}{\|u_1^{(1)}\|_{L^\infty}} + m_u^{(2)} u_1^{(2)}(r,z), \quad \omega_1^0(r,z) = m_\omega^{(1)} \frac{\omega_1^{(1)}(r,z)}{\|\omega_1^{(1)}\|_{L^\infty}} + m_\omega^{(2)} \omega_1^{(2)}(r,z),$$

where

$$\begin{aligned}
u_1^{(1)} &= \frac{\sin(2\pi z)}{1 + (\sin(\pi z)/a_{z1})^2 + (\sin(\pi z)/a_{z2})^4} \cdot \frac{r^8(1-r^2)}{1 + (r/a_{r1})^{10} + (r/a_{r2})^{14}},\\
u_1^{(2)} &= \sin(2\pi z) \cdot r^2(1-r^2),\\
\omega_1^{(1)} &= g(r,z) \cdot \frac{\sin(2\pi z)}{1 + (\sin(\pi z)/b_{z1})^2 + (\sin(\pi z)/b_{z2})^4} \cdot \frac{r^8(1-r^2)}{1 + (r/b_{r1})^{10} + (r/b_{r2})^{14}},\\
\text{and} \quad \omega_1^{(2)} &= \sin(2\pi z) \cdot r^2(1-r^2).
\end{aligned}$$

The parameters are chosen as follows:

$$m_u^{(1)} = 7.6 \times 10^3, \quad m_u^{(2)} = 50, \quad m_\omega^{(1)} = 8.6 \times 10^7, \quad m_\omega^{(2)} = 50,$$
$$a_{z1} = (1.2 \times 10^{-4})\pi, \quad a_{z2} = (2.5 \times 10^{-4})\pi, \quad a_{r1} = 9 \times 10^{-4}, \quad a_{r2} = 5 \times 10^{-3},$$
$$b_{z1} = (1 \times 10^{-4})\pi, \quad b_{z2} = (1.5 \times 10^{-4})\pi, \quad b_{r1} = 9 \times 10^{-4}, \quad b_{r2} = 3 \times 10^{-3}.$$

The function $g(r,z)$ is defined through a soft-cutoff function, and it forces the profile of ω_1^0 to have a smooth "corner" shape. Define the soft-cutoff function

$$f_{sc}(x;a,b) = \frac{e^{(x-a)/b}}{e^{(x-a)/b} + e^{-(x-a)/b}}. \tag{A.2}$$

Then $g(r,z)$ is given by the formula

$$g(r,z) = \big(1 - f_{sc}(\sin(\pi z)/\pi; 0.7b_{z1}, 0.5b_{z1}) \cdot f_{sc}(r; b_{r1} + 0.5b_{z1}, b_{z1})\big)$$
$$\times \big(1 - f_{sc}(-\sin(\pi z)/\pi; 0.7b_{z1}, 0.5b_{z1}) \cdot f_{sc}(r; b_{r1} + 0.5b_{z1}, b_{z1})\big).$$

Moreover, the initial stream function ψ_1^0 is obtained from ω_1^0 via the Poisson equation

$$-\left(\partial_r^2 + \frac{3}{r}\partial_r + \partial_z^2\right)\psi_1^0(r,z) = \omega_1^0(r,z) \quad \text{for } (r,z) \in \mathcal{D}_1,$$

subject to the homogeneous boundary conditions

$$\psi_{1,r}^0(0,z) = \psi_1^0(1,z) = \psi_1^0(r,0) = \psi_1^0(r,1/2) = 0.$$

It is not hard to check that the initial data $u_1^0, \omega_1^0, \psi_1^0$ satisfy all the conditions 1–4. Figure A.1 shows the profiles and contours of the initial data u_1^0 and ω_1^0.

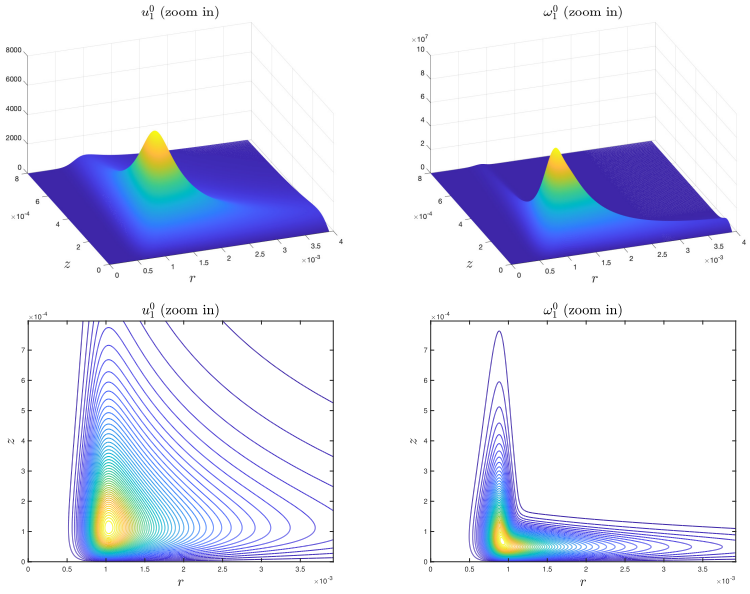

FIG A.1. *Profiles (first row) and contours (second row) of the initial data* u_1^0 *and* ω_1^0 *on a zoom-in domain* $(r,z) \in [0, 4 \times 10^{-3}] \times [0, 8 \times 10^{-4}]$.

As we see in section 3, the solution to the initial-boundary value problem (2.2)–(2.4) and (A.1) develops a potential finite singularity that is focusing at the origin $(r,z)=(0,0)$ and has two separated spatial scales. The sustainability and stability of this two-scale singularity crucially rely on a coupling blowup mechanism that are discussed in detail in section 3.5. Our construction of the initial data serves to trigger this blowup mechanism, owing to the following principles:

- ω_1^0 is chosen to be an odd function of z at $z=0$, so that the angular vorticity $\omega^\theta = r\omega_1$ has a dipole structure on the whole period $\{(r,z) : r \in [0,1], z \in [-1/2,1/2]\}$ that induces a strong inward radial flow near the symmetry plane $z=0$ (see Figure 3.11). This flow structure has the desirable property that pushes the blowing up part of the solution toward the symmetry axis.
- u_1^0 is also chosen to be odd in z at $z=0$, so that the derivative $u_{1,z}^0$ is nontrivial and positive between the maximum point of u_1^0 and $z=0$. As a result, the forcing term $2u_1u_{1,z}$ in the ω_1 equation (2.2b) is positive and large near $z=0$, which contributes to the rapid growth of ω_1.
- For u_1 and ω_1 to have a good initial alignment, we manipulate the initial data so that the maximum point of ω_1^0 is slightly below the maximum point of u_1^0, where $u_{1,z}^0$ large and has the proper sign.
- We scale the magnitude of u_1^0 and ω_1^0 so that $\|\omega_1^0\|_{L^\infty} \approx \|u_1^0\|_{L^\infty}^2$. This is because we have observed the blowup scaling property that $\|\omega_1(t)\|_{L^\infty} \sim \|u_1(t)\|_{L^\infty}^2$ in our computations. The reason behind this blowup scaling property is made clear in section 6.

These principles are critical for the solution to trigger a positive feedback mechanism that leads to a sustainable focusing blowup. We have more discussions on the understanding of this mechanism in section 3.5. We remark that the potential blowup is robust under relatively small perturbation in the initial data. In fact, we have observed similar two-scale blowup phenomena from a family of initial data that satisfy the above properties.

A.2. Variable viscosity coefficients. In our main cases of computation, we choose the variable viscosity coefficients ν^r, ν^z to be the sum of a space-dependent part and a time-dependent part:

$$\nu^r(r,z,t) = \frac{10r^2}{1+10^8r^2} + \frac{10^2(\sin(\pi z)/\pi)^2}{1+10^{11}(\sin(\pi z)/\pi)^2} + \frac{2.5\times 10^{-2}}{\|\omega^\theta(t)\|_{L^\infty}}, \tag{A.3a}$$

$$\nu^z(r,z,t) = \frac{10^{-1}r^2}{1+10^8r^2} + \frac{10^4(\sin(\pi z)/\pi)^2}{1+10^{11}(\sin(\pi z)/\pi)^2} + \frac{2.5\times 10^{-2}}{\|\omega^\theta(t)\|_{L^\infty}}. \tag{A.3b}$$

We remark that the space-dependent parts of ν^r, ν^z are very small (below 10^{-7}) on the whole domain and are of order $O(r^2)+O(z^2)$ for $r \le 10^{-4}$ and $z \le 10^{-5}$. Since the quantity $\|\omega^\theta(t)\|_{L^\infty}$ is growing rapidly in our computation, the time-dependent part in ν^r, ν^z is also very small (below 4×10^{-7} initially) and is decreasing rapidly in time. In fact, the time-dependent part is nonessential for the potential singularity formation in our scenario; it only serves to regularize the solution in the very early stage of our computation and will quickly be dominated by the space-dependent parts. We can even remove the time-dependent part of ν^r, ν^z after the solution enters a stable phase, and the phenomena we observe would remain almost the same.

In all, we only have an extremely weak viscosity effect with smooth degenerate coefficients. Nevertheless, the viscosity plays an important role in the development of the singularity in our blowup scenario. On the one hand, the nontrivial viscosity in the far field prevents the shearing induced instability from disturbing the locally

self-similar solution and the nonlinear alignment of vortex stretching in the near field. On the other hand, we see in section 4 that the degeneracy of the viscosity is crucial for a two-scale singularity to survive in a shrinking domain near the origin $(r,z) = (0,0)$. Furthermore, we argue in section 6 that the order of degeneracy of ν^r, ν^z may contribute to the formation of a potential locally self-similar blowup.

Appendix B. The numerical methods. To numerically compute the potential singularity formation of the equations (2.2), we have designed a composite algorithm that is well-tailored to the solution in our blowup scenario. A more detailed description of our numerical methods is presented in Appendix A of the arXiv version [HH22b] of this paper. Here we summarize the main ingredients of our overall algorithm.

B.1. Adaptive mesh. We see in section 3 that the profile of the solution quickly shrinks in space and develops complex geometric structures, which makes it extremely challenging to numerically compute the solution accurately. In order to overcome this difficulty, we design a special adaptive mesh strategy to resolve the singularity formation near the origin $(r,z) = (0,0)$. More precisely, we construct a pair of mapping functions

$$r = r(\rho), \quad z = z(\eta), \quad (\rho,\eta) \in [0,1] \times [0,1]$$

that maps the square $[0,1] \times [0,1]$ bijectively to the computational domain $\mathcal{D}_1 = \{(r,z) : 0 \le r \le 1, 0 \le z \le 1/2\}$. These mapping functions are dynamically adaptive to the complex multiscale structure of the solution, which is crucial to the accurate computation of the potential singularity. Given a uniform mesh of size $n \times m$ on the $\rho\eta$-domain, the adaptive mesh covering the physical domain is produced as

$$r_i = r(ih_\rho), \quad h_\rho = 1/n; \quad z_j = z(jh_\eta), \quad h_\eta = 1/m.$$

The detailed construction of the mesh mapping functions is described in Appendix B in [HH22b].

B.2. B-spline based Galerkin Poisson solver. One crucial step in our computation is to solve the Poisson problem (2.3c) accurately. The Poisson solver we use should be compatible with our adaptive mesh setting. Moreover, the finite dimensional system of this solver needs to be easy to construct from the mesh, as the mesh is updated frequently in our computation. For these reasons, we choose to implement the Galerkin finite element method based on a tensorization of B-spline functions, following the framework of Luo and Hou [LH14b], who used this method for computing the potential singularity formation of the 3D Euler equations on the solid boundary. The description of the Poisson solver is given in Appendix A.2 in [HH22b].

B.3. Numerical regularization. The potential blowup solution we compute develops a long thin tail structure, stretching from the sharp front to the far field. This tail structure can develop some shearing-induced instability in the late stage of the computation, which may disturb the blowup mechanism. Therefore, we have chosen to apply numerical regularization to stabilize the solution, especially in the tail part. In particular, a low-pass filtering operator with respect to the $\rho\eta$-coordinates is introduced in Appendix A.4 in [HH22b] for our regularization purpose.

B.4. Overall algorithm. We use second-order centered difference schemes for the discretization in space and a second-order explicit Runge–Kutta method for marching the solution in time. Given an adaptive mesh $\mathcal{G}$ and the data (u_1, ω_1)

defined on it, the numerical solution of equations (2.2) is advanced in time via the following procedure.

1. The Poisson equation (2.2c) is solved for ψ_1 using the second-order B-spline based Galerkin method introduced by Luo and Hou in [LH14b].
2. The spacial derivatives are computed using the second-order centered difference schemes and (u^r, u^z) is evaluated at the grid points using (2.2d).
3. An adaptive time stepping δt is computed on $\mathcal{G}$ so that the CFL condition is satisfied with a suitably small CFL number (e.g., 0.1):

$$\delta t_1 = 0.1 \min\left\{ \min_{\rho,\eta} \frac{h_\rho r_\rho}{u^r}, \min_{\rho,\eta} \frac{h_\eta z_\eta}{u^z} \right\} \quad \text{(stability for convection)},$$
$$\delta t_2 = 0.1 \min\left\{ \min_{\rho,\eta} \frac{(h_\rho r_\rho)^2}{\nu^r}, \min_{\rho,\eta} \frac{(h_\eta z_\eta)^2}{\nu^z} \right\} \quad \text{(stability for viscosity)},$$
$$\delta t = \min\{\delta t_1, \delta t_2\}.$$

   We remark that with this choice of δt, the relative growth of the maximum value of the solution in one step is observed to remain below 1%.
4. The solution (u_1, ω_1) is advanced in time by δt using a 2two-stage, second-order explicit Runge–Kutta method.
5. The mesh $\mathcal{G}$ is updated if necessary (see Appendix B in [HH22b]).

We apply the low-pass filtering to mildly regularize the update of the solution in every time step. We have chosen to employ second-order methods since the low-pass filtering scheme we use introduces a second-order error of size $O(h_\rho^2 + h_\eta^2)$. The resulting overall algorithm for solving the initial-boundary value problem (2.2)–(2.4) and (A.1) is formally second-order accurate in space and in time, which will be verified in Appendix C.

Appendix C. Numerical results: Resolution study. In this appendix, we perform a resolution study on the numerical solutions to the initial-boundary value problem (2.2)–(A.1) in Case 1 at various time instants. One can find a more detailed resolution study on all three cases of computation and an investigation on the effectiveness of the adaptive mesh in section 4 in the arXiv version [HH22b] of this paper.

We will estimate the relative error of some solution variable f_p computed on the $256p \times 128p$ mesh by comparing it to a reference variable $\hat{f}$ that is computed on a finer mesh at the same time instant. If f_p is a number, the relative error in absolute value is computed as $e_p = |f_p - \hat{f}|/|\hat{f}|$. If f_p is a spatial function, the reference variable $\hat{f}$ is first interpolated to the mesh on which f is computed. Then the sup-norm relative error is computed as

$$e_p = \frac{\|f_p - \hat{f}\|_\infty}{\|\hat{f}\|_\infty} \quad \text{if } f \text{ is a scalar function}$$
$$\text{and} \quad e_p = \frac{\left\| |(f_p^\theta - \hat{f}_p^\theta, f_p^r - \hat{f}_p^r, f_p^z - \hat{f}_p^z)| \right\|_\infty}{\left\| |(\hat{f}_p^\theta, \hat{f}_p^r, \hat{f}_p^z)| \right\|_\infty} \quad \text{if } f \text{ is a vector function.}$$

For all cases, the reference solution $\hat{f}$ is chosen to be the one computed at the same time instant on the finer mesh of size $256(p+1) \times 128(p+1)$; that is, $\hat{f} = f_{p+1}$. The

numerical order of the error is computed as

$$\beta_p = \log_{\frac{p}{p-1}} \left(\frac{e_{p-1}}{e_p} \right) - 1.$$

Ideally, for a numerical method of order β, the error of a solution variable f_p compared to the ground truth f^* is proportional to $p^{-\beta}$. Suppose that f_p converges to f^* in a monotone fashion; then we should have $e_p \propto p^{-\beta} - (p+1)^{-\beta}$. Substituting this into the formula of β_p yields

$$\beta_p = \log_{\frac{p}{p-1}} \left(\frac{(p-1)^{-\beta} - p^{-\beta}}{p^{-\beta} - (p+1)^{-\beta}} \right) - 1.$$

One can then show that β_p is monotone increasing in p and will converge to the true order β as $p \to \infty$. In particular, for our second-order method, β_p should approach 2 as p increases.

We first study the sup-norm error of the solution, which is the most straightforward indication of the accuracy of our numerical method. Tables C.1–C.4 report the sup-norm relative errors and numerical orders of different solution variables at times

TABLE C.1.
Sup-norm relative errors and numerical orders of u_1, ω_1, ψ_1 at $t = 1.65 \times 10^{-4}$ in Case 1.

Mesh size	Sup-norm relative error at $t = 1.65 \times 10^{-4}$ in Case 1					
	Error of u_1	Order	Error of ω_1	Order	Error of ψ_1	Order
512×256	1.2949×10^{-1}	–	2.7872×10^{-1}	–	2.4290×10^{-2}	–
768×384	4.4825×10^{-2}	1.62	9.8239×10^{-2}	1.57	8.2729×10^{-3}	1.66
1024×512	2.0467×10^{-2}	1.63	4.4789×10^{-2}	1.73	3.8283×10^{-3}	1.68
1280×640	1.1264×10^{-2}	1.68	2.5061×10^{-2}	1.60	1.9905×10^{-3}	1.93
1536×768	7.0304×10^{-3}	1.59	1.5410×10^{-2}	1.67	1.3228×10^{-3}	1.24
1792×896	4.3618×10^{-3}	2.10	9.5333×10^{-3}	2.12	8.2235×10^{-4}	2.08

TABLE C.2.
Sup-norm relative errors and numerical orders of $u^r, u^z, \boldsymbol{\omega}$ at $t = 1.65 \times 10^{-4}$ in Case 1.

Mesh size	Sup-norm relative error at $t = 1.65 \times 10^{-4}$ in Case 1					
	Error of u^r	Order	Error of u^z	Order	Error of $\boldsymbol{\omega}$	Order
512×256	2.3116×10^{-1}	–	6.5401×10^{-2}	–	2.5887×10^{-1}	–
768×384	8.0520×10^{-2}	1.60	2.2632×10^{-2}	1.62	9.1315×10^{-2}	1.57
1024×512	3.6975×10^{-2}	1.71	1.0477×10^{-2}	1.68	4.1456×10^{-2}	1.74
1280×640	2.0084×10^{-2}	1.74	5.7374×10^{-3}	1.70	2.3254×10^{-2}	1.59
1536×768	1.2862×10^{-2}	1.44	3.6477×10^{-3}	1.48	1.4134×10^{-3}	1.73
1792×896	7.9410×10^{-3}	2.13	2.2479×10^{-3}	2.14	8.7579×10^{-3}	2.11

TABLE C.3.
Sup-norm relative errors and numerical orders of u_1, ω_1, ψ_1 at $t = 1.7 \times 10^{-4}$ in Case 1.

Mesh size	Sup-norm relative error at $t = 1.7 \times 10^{-4}$ in Case 1					
	Error of u_1	Order	Error of ω_1	Order	Error of ψ_1	Order
512×256	3.1543×10^{-1}	–	5.7498×10^{-1}	–	6.3176×10^{-2}	–
768×384	1.1080×10^{-1}	1.58	2.1421×10^{-1}	1.44	2.1410×10^{-2}	1.67
1024×512	5.3980×10^{-2}	1.50	1.0487×10^{-1}	1.48	1.0267×10^{-2}	1.55
1280×640	2.8154×10^{-2}	1.92	5.4662×10^{-2}	1.92	5.3087×10^{-3}	1.96
1536×768	1.8674×10^{-2}	1.25	3.6419×10^{-2}	1.23	3.5579×10^{-3}	1.19
1792×896	1.1740×10^{-2}	2.01	2.2894×10^{-2}	2.01	2.2323×10^{-3}	2.02

TABLE C.4.
Sup-norm relative errors and numerical orders of $u^r, u^z, \boldsymbol{\omega}$ at $t = 1.7 \times 10^{-4}$ in Case 1.

Mesh size	Sup-norm relative error at $t = 1.7 \times 10^{-4}$ in Case 1					
	Error of u^r	Order	Error of u^z	Order	Error of $\boldsymbol{\omega}$	Order
512×256	5.1092×10^{-1}	–	1.3200×10^{-1}	–	5.0630×10^{-1}	–
768×384	1.8141×10^{-1}	1.55	4.6313×10^{-2}	1.58	1.8885×10^{-1}	1.43
1024×512	8.8443×10^{-2}	1.50	2.2743×10^{-2}	1.47	9.2927×10^{-2}	1.47
1280×640	4.5596×10^{-2}	1.97	1.2038×10^{-2}	1.85	4.8958×10^{-2}	1.87
1536×768	3.0860×10^{-2}	1.14	7.8363×10^{-3}	1.35	3.2255×10^{-2}	1.29
1792×896	1.9350×10^{-2}	2.03	4.9410×10^{-3}	1.99	2.0271×10^{-2}	2.01

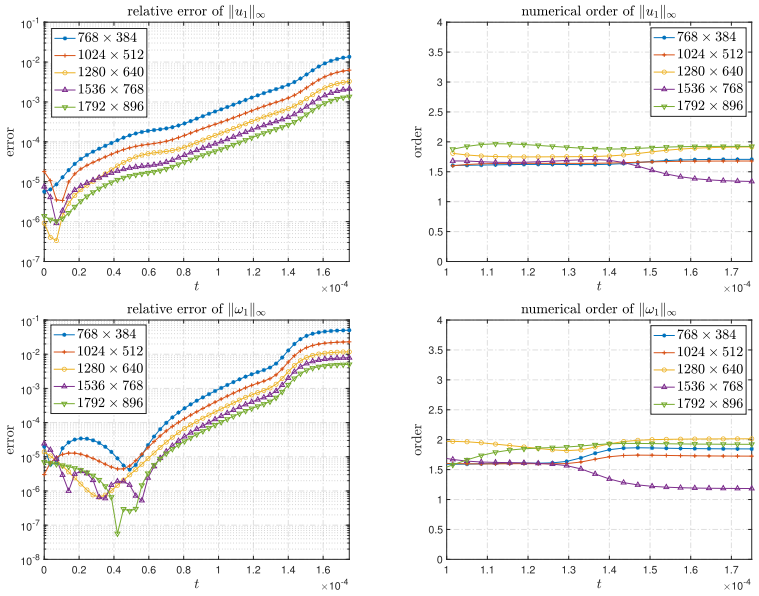

FIG C.1. *First row: relative error and numerical order of $\|u_1(t)\|_{L^\infty}$. Second row: relative error and numerical order of $\|\omega_1(t)\|_{L^\infty}$. The last time instant shown in the figure is $t = 1.76 \times 10^{-4}$.*

$t = 1.65 \times 10^{-4}$ and $t = 1.7 \times 10^{-4}$, respectively. The results confirm that our method in Case 1 is at least second-order accurate. We remark that the error in the solution mainly arises from the interpolation error near the sharp front, where the gradient of the solution is largest and becomes larger and larger in time.

We can also study the convergence of some variables as functions of time. In particular, we report the convergence of the quantities $\|u_1\|_{L^\infty}$, $\|\omega_1\|_{L^\infty}$, $\|\boldsymbol{\omega}\|_{L^\infty}$, and the kinetic energy E. Here the kinetic energy E is given by

$$E := \frac{1}{2}\int_{\mathcal{D}_1} |\boldsymbol{u}|^2 \mathrm{d}x = \frac{1}{2}\int_0^1 \int_0^{1/2} \left(|u^r|^2 + |u^\theta|^2 + |u^z|^2\right) r \, \mathrm{d}r \, \mathrm{d}z.$$

Since the viscosity term with variable coefficients in (2.1) is given in a conservative form, the kinetic energy is a nonincreasing function of time: $E(t_1) \le E(t_2)$ for $t_2 \ge t_1 \ge 0$. Figures C.1 and C.2 plot the relative errors and numerical orders of these quantities as functions of time. The results further confirm that our method is second-order in h_ρ, h_η.

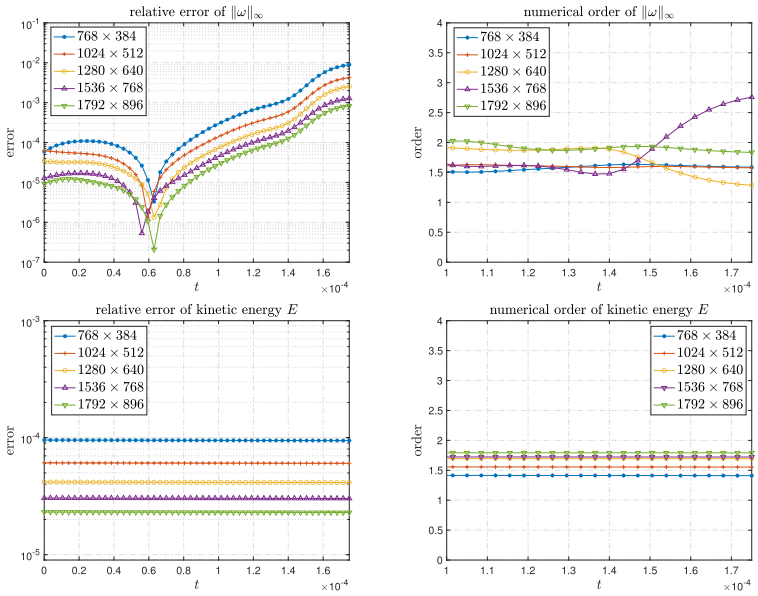

FIG C.2. *First row: relative error and numerical order of* $\|\boldsymbol{\omega}(t)\|_{L^\infty}$. *Second row: relative error and numerical order of* $E(t)$. *The last time instant shown in the figure is* $t = 1.76 \times 10^{-4}$.

On the other hand, we also observe an increasing trend in the relative errors of $\|u_1\|_{L^\infty}$, $\|\omega_1\|_{L^\infty}$, and $\|\boldsymbol{\omega}\|_{L^\infty}$, which implies that our numerical method with a fixed mesh size will not work for all time up to the anticipated singularity. As shown in section 4 of [HH22b], our adaptive mesh strategy may lose its power to resolve the solution as the two scales in the solution become more and more separated. Indeed, the sharp front in the r direction becomes thinner and thinner as t approaches the potential singularity time, which makes it more and more difficult to construct an adaptive mesh with a fixed number of grid points that provides a small approximation error in the entire domain. Therefore, to obtain a well-resolved solution sufficiently close to the potential singularity time, one must use an extremely large number of grid points, which is, unfortunately, beyond the capacity of our current computational resources.

Acknowledgement. We have benefited a lot from AIM SQuaRE, "Towards a 3D Euler Singularity," which has generated many stimulating discussions related to the 3D Euler singularity.

REFERENCES

[BHP16] M. BRENNER, S. HORMOZ, AND A. PUMIR, *Potential singularity mechanism for the Euler equations*, Phys. Rev. Fluids, 1 (2016), 084503.

[BKM84] J. BEALE, T. KATO, AND A. MAJDA, *Remarks on the breakdown of smooth solutions for the 3-D Euler equations*, Commun. Math. Phys., 94 (1984), pp. 61–66.

[BP94] O. N. BORATAV AND R. B. PELZ, *Direct numerical simulation of transition to turbulence from a high-symmetry initial condition*, Phys. Fluids, 6 (1994), pp. 2757–2784.

[CFM96] P. CONSTANTIN, C. FEFFERMAN, AND A. MAJDA, *Geometric constraints on potentially singular solutions for the 3-D Euler equations*, Comm. Partial Differential Equations, 21 (1996), pp. 559–571.

[CH21] J. CHEN AND T. Y. HOU, *Finite time blowup of 2D Boussinesq and 3D Euler equations with* $C^{1,\alpha}$ *velocity and boundary*, Comm. Math. Phys., 383 (2021), pp. 1559–1667.

[CHH21] J. Chen, T. Y. Hou, and D. Huang, *On the finite time blowup of the De Gregorio model for the 3D Euler equations*, Comm. Pure Appl. Math., 74 (2021), pp. 1282–1350.

[CHK+17] K. Choi, T. Y. Hou, A. Kiselev, G. Luo, V. Sverak, and Y. Yao, *On the finite-time blowup of a 1D model for the 3D axisymmetric Euler equations*, Comm. Pure Appl. Math., 70 (2017), pp. 2218–2243.

[DE22] T. D. Drivas and T. M. Elgindi, *Singlarity Formation in the Incompressible Euler Equation in Finite and Infinite Time*, https://arxiv.org/abs/2203.17221v1, 2022.

[DHY05] J. Deng, T. Y. Hou, and X. Yu, *Geometric properties and non-blowup of 3D incompressible Euler flow*, Comm. Partial Differential Equations, 30 (2005), pp. 225–243.

[EGM21] T. M. Elgindi, T.-E. Ghoul, and N. Masmoudi, *Stable self-similar blow-up for a family of nonlocal transport equations*, Anal. PDE, 14 (2021), pp. 891–908.

[Elg21] T. M. Elgindi, *Finite-time singularity formation for $C^{1,\alpha}$ solutions to the incompressible euler equations on $\mathbb{R}^3$*, Ann. of Math., 194 (2021), pp. 647–727.

[ES94] W. E and C.-W. Shu, *Small-scale structures in Boussinesq convection*, Phys. Fluids, 6 (1994), pp. 49–58.

[Gib08] J. Gibbon, *The three-dimensional Euler equations: Where do we stand?*, Phys. D, 237 (2008), pp. 1894–1904.

[GS91] R. Grauer and T. C. Sideris, *Numerical computation of 3D incompressible ideal fluids with swirl*, Phys. Rev. Lett., 67 (1991), pp. 3511–3514.

[HH22a] T. Y. Hou and D. Huang, *A potential two-scale traveling wave asingularity for 3D incompressible Euler equations*, Phys. D, 435 (2022), 133257.

[HH22b] T. Y. Hou and D. Huang, *Potential Singularity Formation of Incompressible Axisymmetric Euler Equations with Degenerate Viscosity Coefficients*, https://arxiv.org/abs/2102.06663, 2022.

[HL06] T. Y. Hou and R. Li, *Dynamic depletion of vortex stretching and non-blowup of the 3-D incompressible Euler equations*, J. Nonlinear Sci., 16 (2006), pp. 639–664.

[HL08a] T. Y. Hou and C. Li, *Dynamic stability of the three-dimensional axisymmetric Navier-Stokes equations with swirl*, Comm. Pure Appl. Math., 61 (2008), pp. 661–697.

[HL08b] T. Y. Hou and R. Li, *Blowup or no blowup? The interplay between theory and numerics*, Phys. D, 237 (2008), pp. 1937–1944.

[HL09] T. Y. Hou and Z. Lei, *On the stabilizing effect of convection in three-dimensional incompressible flows*, Comm. Pure Appl. Math., 62 (2009), pp. 501–564.

[Hou21a] T. Y. Hou, *Potential singularity of the 3D Euler equations in the interior domain*, Found. Comput. Math., https://link.springer.com/article/10.1007/s10208-022-09585-5.

[Hou21b] T. Y. Hou, *The potentially singular behavior of the 3D Navier-Stokes equations*, Found. Comput. Math., https://link.springer.com/article/10.1007/s10208-022-09578-4.

[Ker93] R. M. Kerr, *Evidence for a singularity of the three-dimensional incompressible Eeuler equations*, Phys. Fluids A, 5 (1993), pp. 1725–1746.

[Kis18] A. Kiselev, *Small scales and singularity formation in fluid dynamics*, in Proceedings of the International Congress of Mathematicians, Vol. 3, 2018.

[KRYZ16] A. Kiselev, L. Ryzhik, Y. Yao, and A. Zlatos, *Finite time singularity for the modified SQG patch equation*, Ann. Math., 184 (2016), pp. 909–948.

[KS14] A. Kiselev and V. Sverak, *Small scale creation for solutions of the incompressible two dimensional Euler equation*, Ann. Math., 180 (2014), pp. 1205–1220.

[LH14a] G. Luo and T. Y. Hou, *Potentially singular solutions of the 3D axisymmetric Euler equations*, Proc. Natl Acad. Sci. USA, 111 (2014), pp. 12968–12973.

[LH14b] G. Luo and T. Y. Hou, *Toward the finite-time blowup of the 3D axisymmetric Euler equations: A numerical investigation*, Multiscale Model. Simul., 12 (2014), pp. 1722–1776.

[LW06] J. Liu and W. Wang, *Convergence analysis of the energy and helicity preserving scheme for axisymmetric flows*, SIAM J. Numer. Anal., 44 (2006), pp. 2456–2480.

[MB02] A. Majda and A. Bertozzi, *Vorticity and Incompressible Flow*, Cambridge Texts Appl. Math. 27, Cambridge University Press, Cambridge, UK, 2002.

[PS92] A. Pumir and E. D. Siggia, *Development of singular solutions to the axisymmetric Euler equations*, Phys. Fluids A, 4 (1992), pp. 1472–1491.